Epistemically robust selection of fitted models

Preprint, compiled 23 August, 2024

Alexandre René[*,1, 2, 3] **and André Longtin**[1, 4, 5]

[1]Department of Physics, University of Ottawa, Canada
[2]RWTH Aachen, Fakultät 1, Informatik, Germany
[3]RWTH Aachen, Fakultät 1, Physik, Germany
[4]Department of Cellular and Molecular Medicine, University of Ottawa, Canada
[5]Center for Neural Dynamics, University of Ottawa, Canada

Fitting models to data is an important part of the practice of science, made almost ubiquitous by advances in machine learning. Very often however, fitted solutions are not unique, but form an ensemble of candidate models – *qualitatively* different, yet with comparable *quantitative* performance. One then needs a criterion which can select the best candidate models, or at least *falsify* (reject) the worst ones. Because standard statistical approaches to model selection rely on assumptions which are usually invalid in scientific contexts, they tend to be overconfident, rejecting models based on little more than statistical noise. The ideal objective for fitting models is generally considered to be the *risk*: this is the theoretical average loss of a model (assuming unlimited data). In this work we develop a nonparametric method for estimating, for each candidate model, the *epistemic uncertainty* on its risk: in other words we associate to each model a distribution of scores which accounts for expected *modelling errors*. We then propose that a model falsification criterion should mirror established experimental practice: a falsification result should be accepted only if it is *reproducible* across experimental variations. The strength of this approach is illustrated using examples from physics and neuroscience.

***K*eywords** Model selection, Falsification, Bayes factor, Likelihood ratio, System identification, Empirical model discrepancy, Hierarchical beta process

1 Introduction

Much of our understanding of the natural world is built upon mathematical models. But how we build those models evolves as new techniques and techonologies are developed. With the arrival of machine learning methods, it has become even more feasible to solve inverse problems and learn complex descriptions by applying data-driven methods to scientifically-motivated models [1–3]. However, even moderately complex models are generally *non-identifiable*: many different parameter sets may yield very similar outputs [4–6]. With imperfect real-world data, it is often unclear which – if any – of these models constitutes a trustable solution to the inverse problem.

Non-identifiable models of course predate the current surge of data-driven methods. Already a few decades ago, this was a serious concern within the geosciences, which spurred the development of ensemble methods like GLUE [7–9] and Bayesian calibration [10], where predictions are obtained by averaging over models. Others in that field argued that ontologically it should be preferable to treat the ensemble of identified models as a result in itself: one may apply a falsification criterion to prune the set of plausible models, but attempts at averaging them should be avoided [5].

In this context also emerged the distinction between *aleatoric* and *epistemic* uncertainty [11]. Aleatoric uncertainty is a source of randomness which is accounted for by a model; for example, a model may include a random variable ξ to account for uncertainty in a voltage measurement. *Epistemic* uncertainty is related to the model itself: Should the model include a nonlinear term? Should ξ follow a normal distribution? Should we use parameter set Θ_A or Θ_B? A model's non-identifiability can thus be viewed as a form of epistemic uncertainty.

More recently, this aleatoric-vs-epistemic distinction has improved the framing of uncertainty in other fields, including machine learning [12, 13], astrophysics [14] and condensed matter physics [15]. In these works the learned models are often neural networks, and the epistemic uncertainty is modelled by randomness on the network weights; they are thus also ensemble methods.

Unfortunately, ensemble models are difficult to interpret since they are generally invalid in a Bayesian sense [16]. In light of this, if the goal is to find interpretable models, then an approach like that advocated by Tarantola [5], which aims to identify a finite set of plausible models, seems to us more appropriate. The fact that the number of plausible models is finite (and hopefully small) allows each to be interpreted individually rather than as an ensemble. In this work we design a falsification criterion to determine which models should be part of this plausible set. Model selection is a general problem in computational science, and we will illustrate this criterion using examples from biology and physics.

It may be useful to note that the notion of epistemic uncertainty is closely related to that of *systematic error* or measurement *bias*: if we systematically under or overestimate a measurement, then in some sense our model of how that measurement is taken must be wrong. (Note that the converse is not true: an incorrect model can still lead to unbiased measurements.) For their part, machine learning practitioners may be familiar with the distinction between *in-class* and *out-of-class* inference, the

*Corresponding author: rene@physik.rwth-aachen.de

latter referring to fitting a model to data it would not be able to produce. When we fit a model to out-of-class data assuming it is in-class, we are also making an *epistemic error*. This is often referred to in the literature as *model mismatch*.

The high-level methodology proposed by Tarantola [5] comes down to the following: 1. Construct a (potentionally large) set of *candidate models*. 2. Apply a *falsification criterion* to each candidate model in the set. 3. Retain from the set of candidate models those that satisfy the criterion. Underpinning this procedure is a belief that there exists a true natural process underlying the data, and that with perfect knowledge of that process we could reproduce the data with perfect (statistical) accuracy. It then makes sense to view the multiplicity of plausible models as a reflection of our *epistemic uncertainty*: our lack of knowledge of the true physics and/or measurement process.

Step 1 can be accomplished in different ways; for example, Prinz *et al.* [6] performed a grid search using a model of the lobster's pyloric rhythm, and found thousands of distinct parameter combinations which reproduce chosen features of the recordings. More recently, machine learning methods have also been used to learn rich mechanistic models of molecular forces[1], cellular alignment[3] and neural circuits[2, 17]. Since these are intrinsically nonlinear models, their objective landscape contains a multitude of local minima, which translates to a multitude of candidate models.

The focus of our work is to present a practical criterion for step 2; we therefore assume that we have already obtained a set of candidate models. We make only three hard requirements. First, a candidate model $\mathcal{M}$ must be probabilistic, taking the form

$$p(y_i \mid x_i; \mathcal{M}), \quad (x_i, y_i) \in \mathcal{D}_{\text{test}}, \tag{1}$$

where $\mathcal{D}_{\text{test}}$ is the observed dataset and $(x_i \in \mathbb{R}^n, y_i \in \mathbb{R}^m)$ is the i-th input/output pair (or independent/dependent variables) that was observed. Often this takes the form of a mechanistic model with some additional observation noise. Second, it must be possible to generate arbitrarily many synthetic sample pairs (x, y) following the model's distribution. And third, any candidate model must assign a non-vanishing probability to each of the observations:

$$p(y_i \mid x_i; \Theta) > 0, \quad \forall (x_i, y_i) \in \mathcal{D}_{\text{test}}. \tag{2}$$

For example, a model whose predictions y are restricted to an interval $[a, b]$ is only allowed if all observations are within that interval.

Consider an experiment consisting of measuring the radiation spectrum of a black body as a function of temperature. Taking inspiration from the well-known episode of the "ultraviolet catastrophe", we will use this example in a later section to illustrate our method by comparing two models for the physical process giving rise to this spectrum: the classical Rayleigh-Jeans model $\mathcal{M}_{\text{RJ}}$ and the quantized Planck model $\mathcal{M}_{\text{P}}$. Even though the Planck model is known to be correct, experimental data would not follow the perfect smooth line it predicts. Rather they would be the result of the actual physical process of radiation, *plus* the contamination from any number of noise sources dependent on the experiment details – not to mention variation due to the source not being a perfect black body. In its simplest form this noise may be additive, so that the model may be written as a deterministic function f (depending on the choice of model $\mathcal{M} \in \{\mathcal{M}_{\text{RJ}}, \mathcal{M}_{\text{P}}\}$), plus a random variable ξ affecting the observation:

$$y_i = f(x_i; \mathcal{M}) + \xi_i .$$

(Although omitted here for simplicity, in general ξ may also depend on $\mathcal{M}$.) In such a case, the probability in equation (1) reduces to $p(\xi_i = y_i - f(x_i; \mathcal{M}))$; if ξ_i is Gaussian with variance σ^2, this further reduces to $p(y_i \mid x_i; \mathcal{M}) \propto \exp(-(y_i - f(x_i; \mathcal{M}))^2/2\sigma^2)$. However, in many cases the model itself is stochastic, or the noise is neither additive nor Gaussian. Moreover, even when such assumptions seem justified, we should be able to test them against alternatives.

The selection approach we propose compares pairs of candidate models, without making any assumption on their structure. Two models may be given by two completely different sets of equations, or they may have the same equations but differ only in their parameters, as long as they can be cast in the form of equation (1). In many cases, models will contain a "physical" component – the process we want to describe – and an "observation" component – the unavoidable experimental noise. Distinguishing these components is often useful, but it makes no difference from the point of view of our method: only the combined "physical + observation" model matters.

The *risk* R (defined as the expectation of the loss) is a standard measure of performance used to fit machine learning models: better models have lower risk. Key to our approach however is to compute the risk not as a single value, but as a *risk-* or *R-distribution*, which allows us to represent epistemic uncertainty and generalisation error. Only when two models have sufficiently non-overlapping R-distributions do we say that the one with higher R is *falsified*.

We illustrate most of our results using the neural circuit model of Prinz *et al.* [6] with additive noise. We start by arguing that experimental reproducibility can be equated with statistical robustness. We then use this idea to construct a computable model selection criterion (denoted B^{EMD}) based on the epistemic uncertainty of each model's risk. Here EMD stands for *empirical modelling discrepancy*, which describes the manner in which we estimate epistemic uncertainty. This mainly involves three steps, which are schematically illustrated in Fig. 1. First, we represent the prediction accuracy of each model with a quantile function q^* of the loss. Second, by measuring the self-consistency of q^* with the model's own predictions ($\tilde{q}$), we obtain a measure (δ^{EMD}) of epistemic uncertainty, from which we construct a stochastic process $\mathfrak{Q}$ over quantile functions. Since each realisation of $\mathfrak{Q}$ can be integrated to yield the risk, $\mathfrak{Q}$ thus induces the R-distributions we seek. This requires however the introduction of a new type of stochastic process, which we call *hierarchical beta process*, in order to ensure that realizations are valid quantile functions. The third step is a calibration procedure, where we validate the probability estimated by the B^{EMD} on a set of simulated experiments. To ensure the soundness of our results, we used over 24,000 simulated experiments, across 16 forms of experimental variation.

A defining feature of the B^{EMD} is that it treats the risk as a distribution, which neatly separates the effects of model accuracy from epistemic uncertainty: the former affects the location of the R-distribution, while the latter affects its spread. To illustrate how modelling errors and observation noise interact to affect the selection criteria, we use the aforementioned model

for black body radiation with Poisson noise; this much simpler model allows us to probe this interaction more systematically. Finally, we also compare the B^{EMD} against standard model selection criteria, such as the Akaike information criterion (AIC) or Bayes factors, in an example where two candidate models are difficult to differentiate. We show that the B^{EMD} is less prone than other criteria to show undesirable behaviours such as overconfidence or lack of convergence as the dataset size increases.

2 Results

2.1 Example application: Selecting among disparate parameter sets of a biophysical model

To illustrate our method, we use the dynamical model for a neuron membrane potential described in Prinz *et al.* [6]. This choice was motivated by the fact that fitting a neuron model is a highly ill-posed problem, and therefore corresponds to the situation we set out in the Introduction: disparate sets of parameters which nevertheless produce similar outputs. We will focus on the particular LP neuron type; Prinz *et al.* [6] find five distinct parameter sets which reproduce its experimental characteristics. Throughout this work, we reserve `LP 1` as the model that generates through simulation the *true data* $\mathcal{D}_{\mathrm{test}}$, and use `LP 2` to `LP 5` to define the *candidate models* $\mathcal{M}_A$ to $\mathcal{M}_D$ which we compare against $\mathcal{D}_{\mathrm{test}}$. We intentionally exclude `LP 1` from the candidate parameters to emulate the typical situation where none of the candidate models fit the data perfectly. Visual inspection of model outputs suggests that two candidates (models $\mathcal{M}_A$ and $\mathcal{M}_B$) are more similar to the model output (Fig. 2). We will show that our method is not only consistent with those observations, but makes the similarity between models quantitative.

Remark We denote the dataset $\mathcal{D}_{\mathrm{test}}$ because our work is concerned with distinguishing models after they have been fitted to data. In a typical machine learning pipeline, one splits the data into training and test sets, with the training set used to fit the data (grey faded rectangle in Fig. 1). Since in this work we take fitted models as our starting point, we do not use a training dataset.

The possibility to compare models visually was another factor in choosing this example, since it allows the results to be assessed visually. This allows us to confirm that the method works as expected. Especially for our target application where all candidate models share the same equation structure, a visual validation is key to establishing the soundness of the B^{EMD}, since none of the established model selection like the Bayes factor, AIC or WAIC [19, 20] are applicable. Indeed, these other methods only compare alternative equation structures, not alternative parameter sets. We include a more in-depth comparison to these other methods at the end of the Results.

The datasets in this example take the form of one-dimensional time series, with the time $t \in \mathcal{T}$ as the independent variable and the membrane potential $V^{\mathrm{LP}} \in \mathcal{V}$ as the dependent variable. We denote the space of all possible time-potential tuples $\mathcal{T}\times\mathcal{V}$. Model specifics are given in the Methods; from the point of view of model selection, what matters is that we have ways to generate series of these time-potential tuples: either using the true data-generating process ($\mathcal{M}_{\mathrm{true}}$) or one of the candidate models ($\mathcal{M}_A$ to $\mathcal{M}_D$).

We will assume that the dataset used to evaluate models is composed of L samples, with each sample a $(t, \tilde{V}^{\mathrm{LP}})$ tuple:

$$\mathcal{D}_{\mathrm{test}} = \left\{(t_k, \tilde{V}^{\mathrm{LP}}(t_k; \mathcal{M}_{\mathrm{true}}, I_{\mathrm{ext}})) \in \mathcal{T}\times\mathcal{V}\right\}_{k=1}^{L} . \tag{3}$$

The original model by Prinz *et al.* [6] produced deterministic traces I_{ext}. Experimental measurements however are variable, and our approach depends on that variability. For this work we therefore augment the model with two sources of stochasticity. First, the system as a whole receives a coloured noise input I_{ext}, representing an external current received from other neurons. (External currents may also be produced by the experimenter, to help model the underlying dynamics.) Second, we think of the system as the combination of a biophysical model – described by equations (38) to (40) – and an observation model which adds Gaussian noise. The observation model represents components which don't affect the biophysics – like noise in the recording equipment – and can be modeled to a first approximation as:

$$\tilde{V}^{\mathrm{LP}}(t_k; \mathcal{M}_{\mathrm{true}}) = \underbrace{V^{\mathrm{LP}}(t_k, I_{\mathrm{ext}}(t_k; \tau, \sigma_i); \mathcal{M}_{\mathrm{true}})}_{\text{biophysical model}} + \underbrace{\xi(t_k; \sigma_o)}_{\text{observation model}} . \tag{4}$$

The parameters of the external input I_{ext} are τ and σ_i, which respectively determine its autocorrelation time and strength (i.e. its amplitude). The observation model has only one parameter, σ_o, which determines its scale (specifically its standard deviation). The symbol $\mathcal{M}_{\mathrm{true}}$ is shorthand for everything defining the data-generating process, which includes the parameters τ, σ_i and σ_o. The indices i and o are used to distinguish *input* and *output* model parameters.

To compare the model candidates quantitatively, we take a page from the statistical learning literature: when fitting models to data, define a loss Q and then search for parameters which minimize the expectation of that loss – the *risk* R:

$$R_a := \mathbb{E}_{(t,\tilde{V}^{\mathrm{LP}})\sim\mathcal{M}_{\mathrm{true}}}[Q(t, \tilde{V}^{\mathrm{LP}}; \mathcal{M}_a)] . \tag{5}$$

Here a stands for one of the model labels A, B, C or D. The notation $(t, \tilde{V}^{\mathrm{LP}}) \sim \mathcal{M}_{\mathrm{true}}$ denotes that the distribution from which the observations $(t, \tilde{V}^{\mathrm{LP}})$ are drawn is $\mathcal{M}_{\mathrm{true}}$. We can think of this as producing an infinite sequence of data points by integrating the model dynamics and appyling equation (4) multiple times, or by going to the laboratory and performing the experiment multiple times.

In contrast to the aforementioned model selection criteria (Bayes factor, AIC, WAIC), the risk *is* defined for specific parameter sets with a fixed equation structure, and is the gold standard objective for a machine learning algorithm [21, 22]. (In practice it must be approximated by the *empirical* risk, which is the average of the loss of finitely many samples. In the limit of infinite samples, the empirical risk should converge to the true risk.[21]) The candidate models in this example assume additive observational Gaussian noise, so a natural choice for the loss function is the negative log likelihood:

$$\begin{aligned} Q(t_k, \tilde{V}^{\mathrm{LP}}; \mathcal{M}_a) &= -\log p(\tilde{V}^{\mathrm{LP}} \mid t_k, \mathcal{M}_a) \\ &= \tfrac{1}{2}\log(2\pi\sigma_o) - \frac{(\xi_i)^2}{2\sigma} , \\ &= \tfrac{1}{2}\log(2\pi\sigma_o) - \frac{(\tilde{V}^{\mathrm{LP}} - V^{\mathrm{LP}}(t_k; \mathcal{M}_a))^2}{2\sigma_o} . \end{aligned} \tag{6}$$

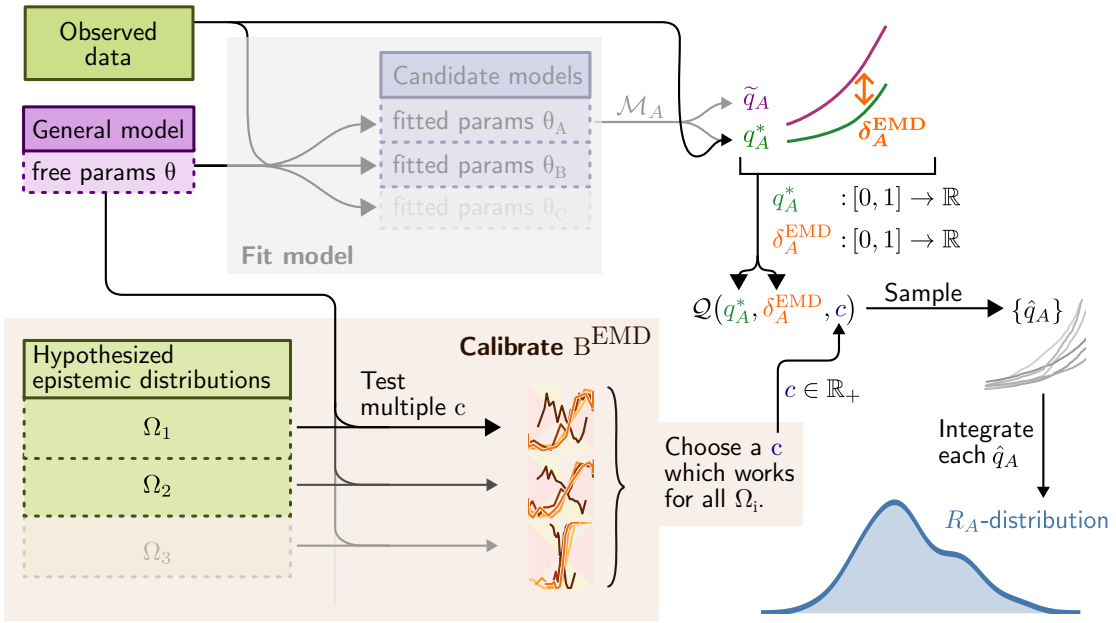

Figure 1: **Overview of the approach for computing *R*-distributions.** We assume the model has already been fitted to obtain a set of *candidate parameter sets* θ_A, θ_B... (Not shown: the models may also be structurally different.) Each candidate parameter set Θ_A defines a *candidate model* $\mathcal{M}_A$, for which we describe the statistics of the loss with two different quantile functions: the purely synthetic $\tilde{q}_A$ which depends only on the model, and the mixed q_A^* which depends on both the model and the data. A small discrepancy δ_A^{EMD} between those two curves indicates that model predictions are consistent with the observed data. Both q_A^* and δ_A^{EMD} are then used to parameterize a stochastic process $\mathfrak{Q}$ which generates random quantile functions. This induces a distribution for the risk R_A of model $\mathcal{M}_A$, which we ascribe to *epistemic uncertainty*. The stochastic process $\mathfrak{Q}$ also depends on a global scaling parameter c. This is independent of the specific model, and is obtained by calibrating the procedure with simulated experiments Ω_i that reflect variations in laboratory conditions. The computation steps on the right (white background) have been packaged as available software [18].

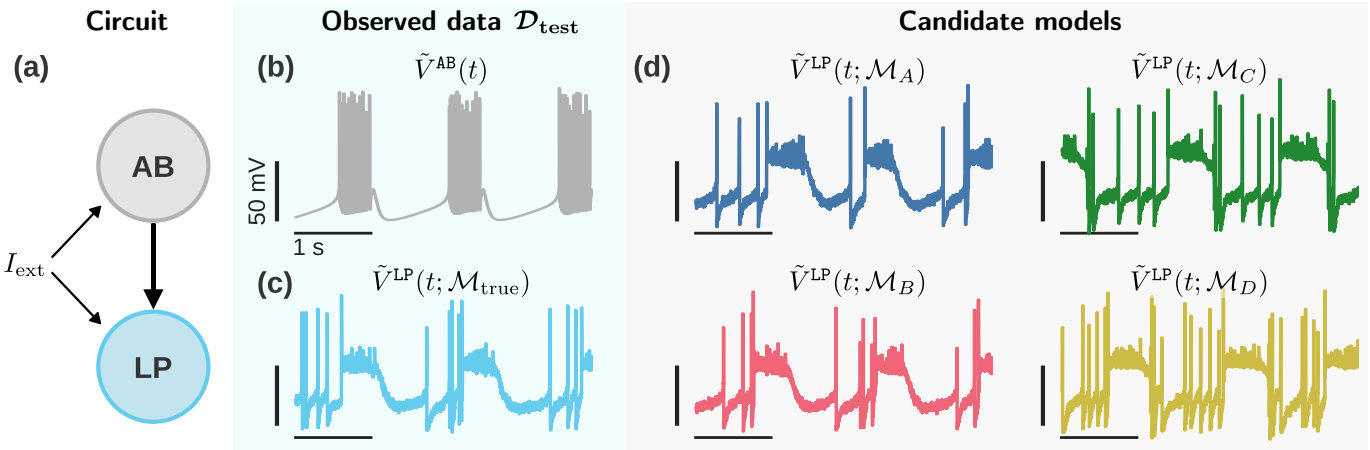

Figure 2: **Comparison of LP neuron responses** The goal is to estimate a good set of candidate models for neuron LP. **a)** We consider a simple circuit with a known pacemaker neuron (AB) and a post-synaptic neuron of unknown response (LP). **b)** Output of the AB neuron. This serves as input to the LP neuron. In practice, these data would more likely be provided by an experimental recording of neuron AB, but here we assume it is a simulatable known model for convenience. **c)** Response of neuron model `LP 1` to the input in (b). Together, (b) and (c) serve as our observed data $\mathcal{D}_{\mathrm{test}}$. **d)** Response of neuron models `LP 2` to `LP 5` to the input in (b). These are our four candidate models of neuron LP.

However one should keep in mind that a) it is not necessary to define the loss in terms of the log likelihood, and b) the loss used to *compare* models need not be the same used to *fit* the models. For example, if the log likelihood of the assumed observation model is non-convex or non-differentiable, one might use a simpler objective for optimization. Alternatively, one might fit using the log likelihood, but compare models based on global metrics like the interspike interval. Notably, Prinz *et al.* [6] do not directly fit to potential traces $\tilde{V}$, but rather use a set of data-specific heuristics and global statistics to select candidate models. In this work we stick with the generic form of equation (6), which makes no assumptions on the type of data used to fit the models and is thus easier to generalise to different scenarios.

As alluded to above, the candidate model traces in Fig. 2**d** suggest two groups of models: the $\mathcal{M}_A$ and $\mathcal{M}_B$ models seem to better reproduce the data than $\mathcal{M}_C$ or $\mathcal{M}_D$. Within each group however, it is hard to say whether one model is better than the other; in terms of the risks, this means that we expect $R_A, R_B < R_C, R_D$. This also means that we should be wary of a selection criterion which unequivocally ranks $\mathcal{M}_A$ better than $\mathcal{M}_B$, or $\mathcal{M}_C$ better than $\mathcal{M}_D$.

In other words we need to associate an uncertainty to the risks R_A to R_D. A traditional way to do this would be with a method like bootstrapping; however this only estimates the aleatoric component of the uncertainty. In the following sections we will show that the aleatoric component vanishes in the large L limit, and therefore that to obtain meaningful uncertainties, we must also estimate their *epistemic* component. We will do this by constructing a special one dimensional stochastic process for quantile functions of the model loss.

2.2 Generalisability, reproducibility and robustness

Evaluating the risk (5) for each candidate model yields four scalars R_A to R_D; since a lower risk should indicate a better model, a simple naive criterion would be

$$B^R_{ab} := \begin{cases} \mathcal{M}_a & \text{if } R_a < R_b\,, \\ \mathcal{M}_b & \text{if } R_b < R_a\,, \\ \text{equivocal} & \text{if } R_a = R_b\,. \end{cases} \qquad \text{for } a, b \in \{A, B, C, D\} \tag{7}$$

Note that this criterion is effectively binary since the third option, "equivocal", has probability zero. It therefore *always* selects either $\mathcal{M}_a$ or $\mathcal{M}_b$, even when the evidence favouring one of the two is extremely weak. Another way to see this is illustrated at the top of Fig. 3: the lines representing the four values R_A through R_D have no error bars, so even minute differences suffice to rank the models.

The problem is that from a scientific standpoint, if the evidence is too weak, this ranking is likely irrelevant – or worse, misinformative. Indeed, the goal of scientific inquiry is to make inferences which generalise beyond the laboratory. Scientific practice has established that a good standard to achieve such inferences is *reproducibility*: the community will only accept a new observation after it has been reproduced in separate experiments, ideally from different groups. This ensures that the observation is robust with respect to at least small variations in the experimental setup.

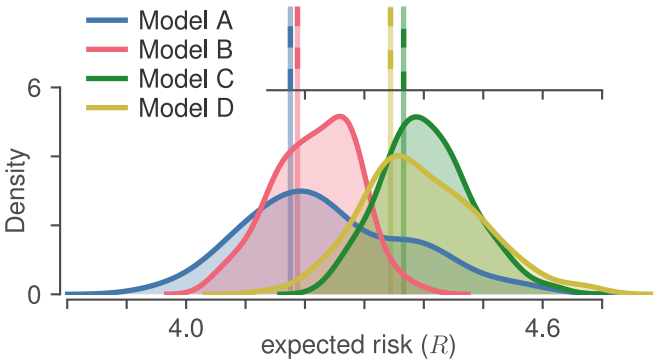

Figure 3: **Risk vs. R-distributions for the four candidate LP models. (top) The risk** (5) for each of the four candidate LP models. **(bottom) Our proposed B^{EMD} criterion** replaces the risk by an *R-distribution*, where the scale of each distribution is due to the *epistemic uncertainty* for that particular model. R-distributions are distributions of the R functional in equation (14); we estimate them by sampling the quantile function (i.e. inverse cumulative density function) q according to a stochastic process $\mathfrak{Q}$ on quantile functions. In contrast to the distributions in Fig. 4, they do not collapse in the limit of infinite data unless the epistemic uncertainty is zero. We used an EMD sensitivity constant of $c = 2^{-2}$ for $\mathfrak{Q}$ and drew samples $\hat{q} \sim \mathfrak{Q}$ until the relative standard error on the risk was below 3 %. A kernel density estimate (KDE) is used to display those samples as distributions.

We can translate this idea to the problem of model selection by treating the outcome of the selection as our "observation". In turn, "reproducing" an experiment implies at least small changes in the way data are generated. In more statistical terms therefore, we require that *the decision to falsify a model should be robust with respect to small changes in* $\mathcal{M}_{\text{true}}$.

In contrast to the naive B^R criterion of equation (7), model selection criteria are typically not binary, but take real values which purportedly represent the strength of the evidence for or against a model. For example, a Bayes factor is interpreted as the ratio of probabilities $P(\mathcal{M}_A)/P(\mathcal{M}_B)$: if this ratio is too close to 1, the comparison is equivocal. For a good selection criterion, when the reported evidence strength is high, the outcome of the comparison (which model is selected) should be robust. On the other hand, when the reported evidence is weak (e.g. a Bayes factor close to 1), it does not matter which model it selects. To summarize:

$$\begin{aligned} \text{Reported} \\ \text{strong evidence} \end{aligned} \Rightarrow \begin{aligned} \text{Model selection} \\ \text{outcome is robust} \end{aligned} \qquad \begin{aligned} \text{Reported} \\ \text{weak evidence} \end{aligned} \Rightarrow \begin{aligned} \text{Inconsequential} \\ \text{(no model selected)} \end{aligned} \tag{8}$$

In the following we call criteria which do *not* satisfy this requirement *overconfident*, since they overestimate the strength of their evidence. Unfortunately, commonly used model selection criteria – including the likelihood ratio, AIC and WAIC – are overconfident when the dataset becomes large. We give an example of this in Table 2 .

The idea that robustness against experimental variations may be a logical keystone for translating machine learning results into scientific conclusions has also emerged in other recent work [23, 24]. There, as here, the precise definition of a "distribution over models" is left to the practitioner, since appropriate choices will depend on the application. This is not unreasonable: a falsification decision should not be too sensitive to the choice of this distribution, exactly because it should be robust. In the following we use Ω to denote a distribution over models.

To illustrate using our example, consider that the input I_{ext} and noise ξ might not be stationary over the course of an experiment with multiple trials. Or alternatively, different datasets might come from different laboratories. We can represent this by making their parameters random variables, for example

$$\Omega := \begin{cases} \log \sigma_o \sim \mathcal{N}(0.0\,\text{mV}, (0.5\,\text{mV})^2) \\ \log \sigma_i \sim \mathcal{N}(-15.0\,\text{mV}, (0.5\,\text{mV})^2) \\ \log_{10} \tau \sim \text{Unif}([0.1\,\text{ms}, 0.2\,\text{ms}]) \end{cases} , \tag{9}$$

and drawing new values of $(\sigma_o, \sigma_i, \tau)$ for each trial. Since it is a distribution over data-generating processes, we call Ω an *epistemic distribution*. An epistemic distribution is a way of representing epistemic *uncertainty* as an explicit distribution over processes. For illustration purposes, here we have parameterized Ω in terms of two parameters of the biophysical model and one parameter of the observation model, thus capturing epistemic uncertainty within a single experiment. In general the parameterization of Ω is a modelling choice, and may represent other forms of uncertainty – for example due to variations between experimental setups in different laboratories.

Conceptually, we could test the robustness of a criterion by generating different "true models" $\mathcal{M}'_{\text{true}}$ by sampling from Ω, for each then drawing a dataset $\mathcal{D}'_{\text{test}} \sim \mathcal{M}'_{\text{true}}$, and then finally computing the model selection criteria for each dataset. However, if we want to select models based on how well they fit the *actual* data D_{test}, we cannot use hypothetical datasets $\mathcal{D}'_{\text{test}}$ – we need to use the observed data $\mathcal{D}_{\text{test}}$, for which we *don't* know $\mathcal{M}_{\text{true}}$ unless the data are synthetic. Therefore in the next sections we propose a different type of distribution which is over risks R (in contrast to an epistemic distribution, which is over data-generating models, each with its own parameter set); we call this an *R-distribution*. This is a non-parametric distribution constructed to account for the mismatch between model and data, which avoids the need to explicitely specify possible variations as we did in equation (9).

Both epistemic distributions Ω and R-distributions are ways to represent epistemic uncertainty, but the latter being lower-dimensional and more abstract is what allows us to construct them non-parametrically. On the other hand an epistemic distribution is more easily interpreted, a property we use below to define a calibration and validation procedure for the B^{EMD}.

Before continuing, we want to stress that although it may look like one, an epistemic distribution is *not a prior distribution*: in a Bayesian calculation, there can only be one prior since it appears in the calculation of the posterior. Here we can define as many epistemic distributions as we want, since they serve only to validate the R-distributions. (The opposite however holds: a prior can be viewed as a particular choice of epistemic distribution.)

2.3 Model discrepancy as a baseline for epistemic uncertainty

To keep the notation in the following sections more general, we use the generic x and y as independent and dependent variables. To recover expressions for our neuron example, substitute $x \to t$, $y \to \tilde{V}^{\text{LP}}$, $\mathcal{X} \to \mathcal{T}$ and $\mathcal{Y} \to \mathcal{V}$. Where possible we also use A and B as a generic placeholder for a model label.

Our goal is to define a notion of robustness against epistemic variations which can be computed *using knowledge only of the candidate models and the observed empirical data*. We do this by quantifying the discrepancy between model predictions and observations: this establishes a lower bound for the epistemic uncertainty, since it must be at least large enough to account for the discrepancy. We then construct a stochastic process to explain the discrepancy, and therefore the corresponding epistemic uncertainty.

More concretely, in the next section we define the discrepancy function δ_A^{EMD} to quantify the difference between predictions of a model $\mathcal{M}_A$ and the actual observed data $\mathcal{D}_{\text{test}}$; EMD stands for *empirical model discrepancy*. We use δ_A^{EMD} to induce a distribution on the risk R_A (Fig. 3, bottom). An R-distribution defined this way only accounts for the minimal amount of epistemic uncertainty required to explain the mismatch between the data and the model; it does not account for additional sources of variation such as repeating the experiment under different conditions.

Given such distributions for the risk of each model, we then define the $B^{\text{EMD}}_{AB;c}$ criterion comparing two models $\mathcal{M}_A$ and $\mathcal{M}_B$ as

$$B^{\text{EMD}}_{AB;c} := P(R_A < R_B \mid c)\,. \tag{10}$$

The parameter $c \in \mathbb{R}_+$, which is explained in the section listing desiderata for $\mathfrak{Q}$, allows a practitioner to adjust the sensitivity of the criterion to modelling errors. A practitioner must also select a *falsfication threshold* $\epsilon \in (0, 1)$; a model A is then said to be falsified (with confidence ϵ) if there exists another model B for which $B^{\text{EMD}}_{AB;c} < \epsilon$.

By construction equation (10) satisfies the requirement that strong evidence implies robust model selection equation (8), since B^{EMD}_{AB} is near 0 or 1 only when the outcome of the comparison is robust. Table 1 gives the value of B^{EMD} for each candidate model pair in our example from Figs. 2 and 3. As expected, models that were visually assessed to be similar also have B^{EMD} values close to $\frac{1}{2}$. In practice one would not necessarily need to compute the entire table, since the B^{EMD} satisfy *dice transitivity* [25, 26]. In particular this implies that

$$\left.\begin{aligned} B^{\text{EMD}}_{AB;c} &> \varphi^{-1} \\ B^{\text{EMD}}_{BC;c} &> \varphi^{-1} \end{aligned}\right\} \Rightarrow B^{\text{EMD}}_{AC;c} < \varphi^{-1}\,, \tag{11}$$

where φ is the golden ratio; therefore as long as we set the falsification threshold larger than $\varphi^{-1} \approx 0.62$, we can treat model comparisons as transitive. We explain this result in the Supplementary Methods.

We stress that the R-distributions shown in Fig. 3 are not simply distributions of the loss for individual datapoints (i.e. the distribution of $\{Q_a(x, y)\}_{(x,y)\sim\mathcal{D}_{\text{test}}}$). For well-fitted models, such distributions generally show very large overlap, and thus on their own are not particularly useful for comparing models (Fig. 4**a**).

Table 1: **Comparison of B^{EMD} probabilities for candidate LP models.** Values are the probabilities given by equation (10) with the candidate labels a and b corresponding to rows and columns respectively. Candidate models being compared are those of Fig. 2. Probabilities are computed for the R-distributions shown in Fig. 3, which used an EMD constant of $c = 2^{-2}$. Since $P(R_a < R_b) = 1 - P(R_b < R_a)$, the sum of symmetric entries equals 1.

	A	B	C	D
A	0.500	0.483	0.846	0.821
B	0.517	0.500	0.972	0.940
C	0.154	0.028	0.500	0.463
D	0.179	0.060	0.537	0.500

The R-distributions are also qualitatively different from the uncertainty one would estimate with bootstrapping. A bootstrap procedure aims to estimate the uncertainty on a statistic (here the risk R) on a single dataset $\mathcal{D}$ by recomputing it on multiple surrogate datasets obtained by resampling $\mathcal{D}$ with replacement. The variability of the statistic on these copies is therefore an estimate of the *aleatoric* uncertainty due to *the finite dataset size* L – in the limit of infinite data, bootstrap distributions always collapse onto a precise value, no matter the model mismatch; Fig. 4**b** illustrates this dependence of bootstrap estimates on L. In contrast, because they depend on the model mismatch, the distributions in Fig. 3 do not collapse when $L \to \infty$.

Another way to estimate aleatoric uncertainty, when we have access to good candidate models, is to use those models as simulators to generate multiple synthetic datasets. The distribution of risks over those datasets is then a direct estimate of its aleatoric uncertainty. Of course, since the same model is used to generate the data and to evaluate the loss, such an estimate ignores any mismatch between the real and synthetic datasets, and it remains a finite-size effect: as long as the data distribution is stationary, these uncertainties eventually vanish with large enough datasets. We illustrate this in Fig. 4**c**.

In general, for models with stationary data distributions, aleatoric uncertainty can be equated to that uncertainty which vanishes in the limit of infinite data – indeed some authors define it this way [13]. Epistemic uncertainty in contrast can only be reduced by improving a model. For this reason we focus in this work on estimating the epistemic uncertainty on R, although in practice one is likely to estimate both.

2.4 δ^{EMD}: Expressing model-mismatch as a discrepancy between CDFs

We can treat the loss function for a given model $\mathcal{M}_A$ as a random variable $Q(x, y; \mathcal{M}_A)$ where the (x, y) are sampled from $\mathcal{M}_{\text{true}}$. A key realization for our approach is that *the CDF (cumulative distribution function) of the loss suffices to compute the risk*. Indeed, we have for the CDF of the loss

$$\begin{aligned}\Phi_A^*(q) &:= p(Q(x, y; \mathcal{M}_A) \leq q \mid x, y \sim \mathcal{M}_{\text{true}}) \\ &= \int_{\mathcal{X}\times\mathcal{Y}} H(q - Q(x, y; \mathcal{M}_A))\, p(x, y \mid \mathcal{M}_{\text{true}})\, dxdy \\ &\approx \frac{1}{L} \sum_{x,y\in\mathcal{D}_{\text{test}}} H(q - Q(x, y; \mathcal{M}_A))\,, \end{aligned} \tag{12}$$

where H is the Heaviside function.

Since $\mathcal{M}_{\text{true}}$ is unknown, a crucial feature of equation (12) is that $\Phi_A^*(q)$ can be estimated without needing to evaluate $p(x, y \mid \mathcal{M}_{\text{true}})$; indeed, all that is required is to count the number of observed data points in $\mathcal{D}_{\text{test}}$ which according to $\mathcal{M}_A$ have a loss less than q. Moreover, since Q returns a scalar, the data points (x, y) can have any number of dimensions, and the number of data points required to get a good estimate of $\Phi_A^*(q)$ does not depend on the dimensionality of the data – for the same reason that estimating marginals of a distribution requires much fewer samples than estimating the full distribution. Finally, because the loss is evaluated using $\mathcal{M}_A$, but the expectation is taken with respect to a distribution determined by $\mathcal{M}_{\text{true}}$, we call Φ_A^* the *mixed CDF*.

We can invert Φ_A^* to obtain the *mixed PPF* (*percent point function*, also known as *quantile function*, or *percentile function*):

$$q_A^*(\Phi) := {\Phi_A^*}^{-1}(\Phi)\,, \qquad (13, \textit{mixed PPF})$$

which is also a 1-d function, irrespective of the dimensionality of $\mathcal{X}$ or $\mathcal{Y}$. We can then rewrite the risk as a one dimensional integral in q_A^*:

$$\begin{aligned} R_A = R[q_A^*] &= \int_0^1 q_A^*(\Phi)\, d\Phi \\ &\approx \frac{1}{L} \sum_{x,y\in\mathcal{D}_{\text{test}}} Q(x_i, y_i; \mathcal{M}_A)\,. \end{aligned} \tag{14}$$

To obtain equation (14), we simply used Fubini's theorem to reorder the integral of equation (12) and marginalized over all slices of a given loss $q_A^*(\Phi)$. The integral form (first line of equation (14)) is equivalent to averaging an infinite number of samples, and therefore to the *(true) risk*, whereas the average over observed samples (second line of equation (14)) is exactly the definition of the *empirical risk*. (See text leading to equation (6).) Using the latter adds some amount of aleatoric uncertainty to our estimate of R_A, but for large enough datasets this is negligible compared to the epistemic uncertainty. (Compare the epistemic distributions of Fig. 3 with the aleatoric ones of Fig. 4**b**.)

In practice, to evaluate equation (14), we use the observed samples to compute the sequence of per-sample losses $\{Q(x, y; \mathcal{M}_A)\}_{x,y\in\mathcal{D}_{\text{test}}}$. This provides us with a sequence of losses, which we use as ordinate values. We then sort this sequence so that we have $\{Q_i\}_{i=1}^L$ with $Q_i \leq Q_i + 1$, and assign to each the abscissa $\Phi_i = i/L + 1$, such that losses are motonically increasing and uniformly distributed on the [0, 1] interval. This yields the *empirical PPF of the loss* – the "empirical" qualifier referring to this construction via samples, as opposed to an analytic calculation. Interpolating the points then yields a continuous function which can be used in further calculations.

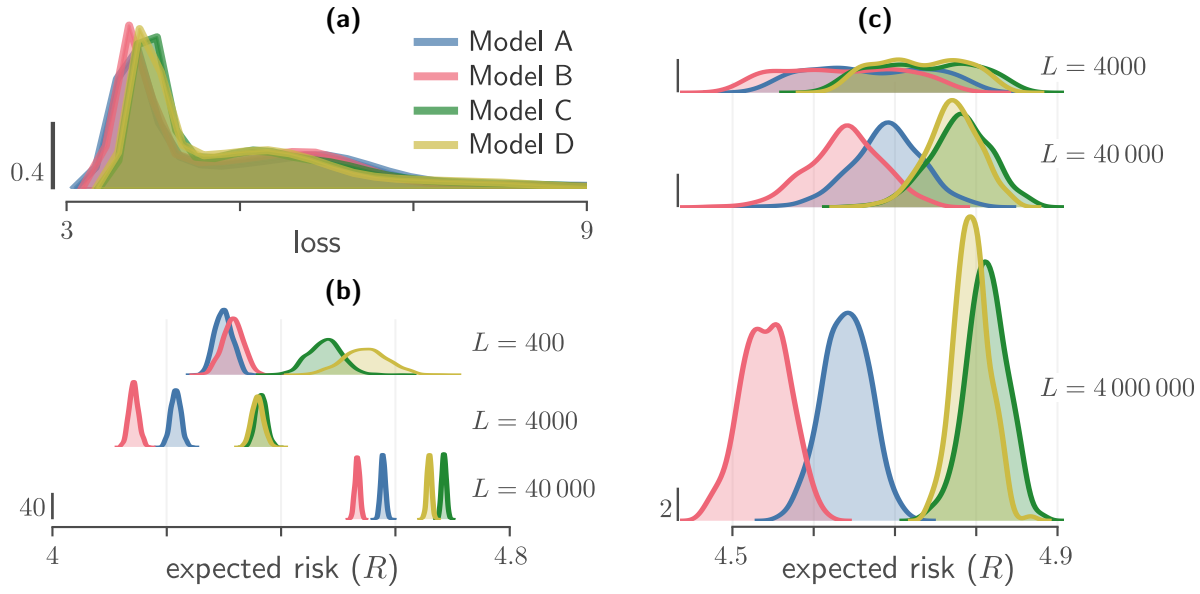

Figure 4: **Aleatoric uncertainty cannot substitute epistemic uncertainty. a) Loss distribution** of individual data points – $\{Q_a(t_k, V^{\mathrm{LP}}(t_k; \mathcal{M}_{\mathrm{true}}))\}$ – for the dataset and models shown in Fig. 2. **b) Bootstrap aleatoric uncertainty** on the risk, obtained using case resampling [27]: for each model, the set of losses was resampled 1200 times with replacement. Dataset and colours are the same as in (a). **c) Synthetic aleatoric uncertainty** on the risk, obtained by evaluating equation (5) on 400 different simulations of the candidate model (differing by the random seed). Here the same model is used for simulation and loss evaluation. Dataset sizes L determine the integration time, adjusted so all datasets contain the same number of spikes. All subpanels use the same vertical scale. **b–c)** The variance of the R-distributions, i.e. the uncertainty on R, goes to zero as L is increased. **a–c)** Colours indicate the model used for the loss. Probability densities were obtained by a kernel density estimate (KDE).

All examples in this paper linearly interpolate the PPF from $2^{10} = 1024$ points.

In Fig. 5 we show four examples of empirical PPFs, along with their associated empirical CDFs. We see that the statistics of the additive observational noise affects the shape of the PPF: for noise with light tails, as we get from Gaussian or Poisson distributions, we have strong concentration around the minimum value of the loss followed by a sharp increase at $\Phi = 1$. For heavier-tailed distributions like Cauchy, loss values are less concentrated and the PPF assigns non-negligible probability mass to a wider range of values. The dimensionality of the data also matters. High-dimensional Gaussians are known to place most of their probability mass in a thin shell centered on the mode, and we see this in the fourth column of Fig. 5: the sharp increase at $\Phi = 0$ indicates that very low probability is assigned to the minimum loss.

Since by construction, the abscissae Φ of an empirical PPF are spaced at intervals of $1/L$, the Riemann sum for the integral in equation (14) reduces to the sample average. More importantly, we can interpret the risk as a functional in $q_A^*(\Phi)$, which will allow us below to define a generic stochastic process that accounts for epistemic uncertainty.

Up to this point with equation (14) we have simply rewritten the usual definition of the risk. As argued at the beginning of the previous section, epistemic uncertainty should, at a minimum, account for discrepancies between the candidate model $\mathcal{M}_A$ and the actual data generating process $\mathcal{M}_{\mathrm{true}}$; specifically we want to account for discrepancies *in the statistics of the loss*. We can do this because $\mathcal{M}_A$ is itself a probabilistic model (recall equation (1)), and therefore we can compute the PPF of $Q(x, y; \mathcal{M}_A)$ under its own model:

$$\begin{aligned}\widetilde{\Phi}_A(q) &:= p(Q(x,y;\mathcal{M}_A) \le q \mid x,y \sim \mathcal{M}_A) \\ &= \int_{\mathcal{X}\times\mathcal{Y}} dxdy\; H(q - Q(x,y;\mathcal{M}_A))\, p(x,y \mid \mathcal{M}_A) \\ &\approx \frac{1}{L_{\mathrm{synth},A}} \sum_{x,y\in\mathcal{D}_{\mathrm{synth},A}} H(q - Q(x,y;\mathcal{M}_A))\,, \end{aligned} \tag{15}$$

from which we obtain the PPF:

$$\tilde{q}_A(\Phi) := \widetilde{\Phi}_A^{-1}(\Phi)\,. \tag{16, *synth PPF*}$$

The only difference between $\tilde{q}_A$ and q_A^* is the use of $p(x, y \mid \mathcal{M}_A)$ instead of $p(x, y \mid \mathcal{M}_{\mathrm{true}})$ in the integral. In practice this integral would also be evaluated by sampling, using $\mathcal{M}_A$ to generate a dataset $\mathcal{D}_{\mathrm{synth},A}$ with $L_{\mathrm{synth},A}$ samples. Because in this case the candidate model is used for both generating samples and defining the loss, we call $\tilde{q}_A$ ($\widetilde{\Phi}_A$) the *synthetic PPF* (*CDF*).

The idea is that the closer $\mathcal{M}_A$ is to $\mathcal{M}_{\mathrm{true}}$, the closer also the synthetic PPF should be to the mixed PPF. Indeed, equality of the PPFs ($\tilde{q}_a = q_A^*$) is a necessary condition for equality of the models ($\mathcal{M}_A = \mathcal{M}_{\mathrm{true}}$). To make this quantitative, we define the discrepancy function $\delta_A^{\mathrm{EMD}}(\Phi)$ as the absolute difference between $\tilde{q}_A$ and q_A^*:

$$\begin{aligned}\delta_A^{\mathrm{EMD}} &: [0,1] \to \mathbb{R} \\ &\Phi \mapsto \left|\tilde{q}_A(\Phi) - q_A^*(\Phi)\right|. \end{aligned} \tag{17}$$

We refer to this function as the *empirical model discrepancy* (EMD) function because it measures the discrepancy between two empirical PPFs.

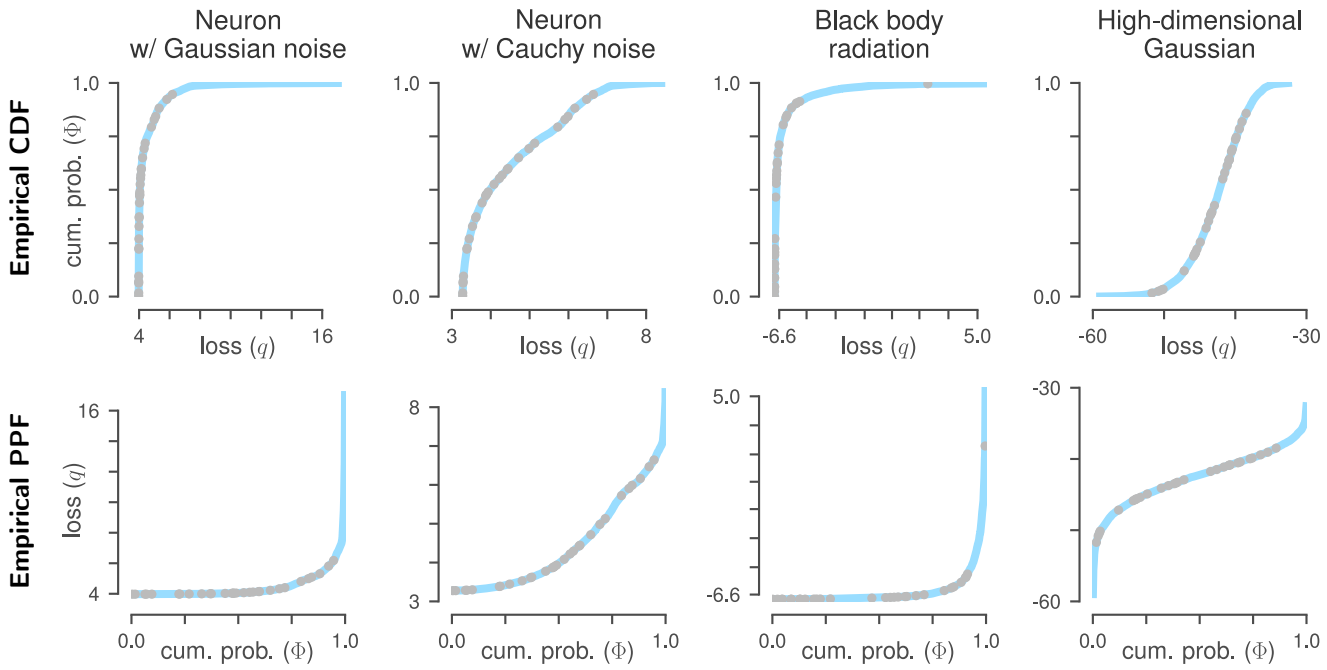

Figure 5: **Loss PPF for different models:** each column corresponds to a different model. The PPF (bottom row) is the inverse of the CDF (top row). For calculations we interpolate $2^{10} = 1024$ points (cyan line) to obtain a smooth function; for illustration purposes here only 30 points are shown. The data for the first two columns were generated with the neuron model described at the top of our Results, where the additive noise follows either a Gaussian or Cauchy distribution. The black body radiation data for the third column were generated from a Poisson distribution using equation (32) with $s = 2^{14}$ and λ in the range 6 µm to 20 µm. Here the true noise is binomial, but the loss assumes a Gaussian. The fourth column shows an example where the data are high-dimensional; the same 30 dimensional, unit variance, isotropic Gaussian is used for both generating the data and evaluating the loss. In all panels the loss function used is the log likelihood under the model.

A non-zero δ_A^{EMD} therefore must be due to a combination of modelling error (i.e. epistemic uncertainty) and finite-size (aleatoric) variations. We can neglect the latter, since a) finite-size effects become negligeable with large enough datasets, and b) doing so is akin to making the worst-case assumption that all discrepancies are due to modelling errors.

2.5 $\mathfrak{Q}$: A stochastic process on quantile functions

In the presence of uncertainty, the PPF of a model is best represented not as a single function, but as a stochastic process on the interval [0, 1]. We write $\mathfrak{Q}_A$ for the stochastic process associated to $\mathcal{M}_A$, and $\hat{q}_A$ for one of its realizations. The realizations $\hat{q}_A$ correspond to "plausible" PPFs for the model $\mathcal{M}_A$ given the observed data; making the idea of plausibility precise, by way of a definition of $\mathfrak{Q}_A$, is the goal of this section. We do this by first establishing a set of desiderata, and then constructing a process $\mathfrak{Q}_A$ which satisfies them. Sampling an ensemble of $\hat{q}_A$ from $\mathfrak{Q}_A$ provides a concrete description of the uncertainty at the level of PPFs; from these we obtain the R-distributions shown in Fig. 3 which are used to compute the $B^{\mathrm{EMD}}_{AB;c}$ criterion equation (10). Schematically, these steps are represented by downward facing arrows on the right of Fig. 1.

It is worth recognising that the task of defining $\mathfrak{Q}_A$ is made considerably simpler by the fact that $\mathfrak{Q}_A$ is always a scalar process, irrespective of the model or dataset.

In defining $\mathfrak{Q}_A$, one must take care that the quantities used to parameterize $\mathfrak{Q}_A$ are in line with the goal of quantifying the epistemic uncertainty on R_A. For example, one might be tempted to set the variance of $\mathfrak{Q}_A$ based on the variance between subsamples of the dataset, in other words via a bootstrapping procedure. However, as already discussed, bootstrapping can only measure *aleatoric* uncertainty. This is why in this section we instead use δ_A^{EMD} to define the variance of $\mathfrak{Q}_A$.

2.5.1 *Desiderata for* $\mathfrak{Q}$

For a realization $\hat{q}_A \sim \mathfrak{Q}_A$ to be plausible, it must be interpretable as a PPF, and it should be "close" to q_A^*. Interpretability as a PPF places quite strong constraints on the realizations, for example:

- All realizations $\hat{q}_A(\Phi) \sim \mathfrak{Q}_A$ must be *monotone*.
- All realizations $\hat{q}_A(\Phi) \sim \mathfrak{Q}_A$ must be *integrable*.

Monotonicity follows immediately from definitions: a CDF is always monotone because it is the integral of a positive function (equation (12)), and therefore its inverse must also be monotone.

Integrability simply means that the integral in equation (14) exists and is finite. Concretely this is enforced by ensuring that the process $\mathfrak{Q}_A$ is *self-consistent* [28], a property which we explain in the Methods.

Interpreting the realizations $\hat{q}$ as PPFs also imposes a third constraint, more subtle but equally important:

- The process $\mathfrak{Q}_A$ must be *non-accumulating*.

A process which is accumulating would start at one end of the domain, say $\Phi = 0$, and sequentially accumulate increments until it reaches the other end. Brownian motion over the interval $[0, T]$ is an example of such a process. In contrast, consider the process of constructing a PPF for the data in Fig. 2: initially we have few data points and the PPF of their loss is very coarse. As the number of points increases, the PPF gets refined, but since loss values occur in no particular order, this happens *simultaneously across the entire interval*.

The accumulation of increments strongly influences the statistics of a process; most notably, the variance is usually larger further along the domain. This would not make sense for a PPF: if $\mathbb{V}[\mathfrak{Q}_A(\Phi)]$ is smaller than $\mathbb{V}[\mathfrak{Q}_A(\Phi')]$, that should be a consequence of $\delta^{\mathrm{EMD}}(\Phi)$ being smaller than $\delta^{\mathrm{EMD}}(\Phi')$ – not of Φ occurring "before" Φ'.

This idea that a realization $\hat{q}_A(\Phi)$ is generated simultaneously across the interval led us to define $\mathfrak{Q}_A$ as a sequence of *refinements*: starting from an initial increment $\Delta\hat{q}_1(0) = \hat{q}_A(1) - \hat{q}_A(0)$ for the entire Φ interval [0, 1], we partition [0, 1] into n subintervals, and sample a set of n subincrements in a way that they sum to $\Delta\hat{q}_1(0)$. This type of distribution, where n random variables are drawn under the constraint of a fixed sum, is called a *compositional* distribution [29]. Note that the constraint reduces the number of dimensions by one, so a pair of increments would be drawn from a 1-d compositional distribution. A typical 1-d example is the beta distribution for $x_1 \in [0, 1]$, with $x_2 = (1 - x_1)$ and $\alpha, \beta > 0$:

$$\text{if } \; x_1 \sim \mathrm{Beta}(\alpha, \beta)\,, \qquad \text{then } \; p(x_1) \propto x_1^{\alpha-1}(1 - x_1)^{\beta-1}\,. \tag{18}$$

Interestingly, the most natural statistics for compositional distributions are not the mean and variance, but analogue notions of *centre* and *metric variance* [29, 30]; for the beta distribution defined above, these are

$$\mathbb{E}_a[(x_1, x_2)] = \frac{1}{e^{\psi(\alpha)} + e^{\psi(\beta)}}(e^{\psi(\alpha)}, e^{\psi(\beta)})\,, \tag{19a}$$

$$\mathrm{Mvar}[(x_1, x_2)] = \frac{1}{2}(\psi_1(\alpha) + \psi_1(\beta))\,, \tag{19b}$$

where ψ and ψ_1 are the digamma and trigamma functions respectively, and $\mathbb{E}_a$ denotes expectation with respect to the Aitchison measure [29, 31]. In essence, equations (19a) and (19b) are obtained by mapping x_1 and x_2 to the unbounded domain $\mathbb{R}$ via a logistic transformation, then evaluating moments of the unbounded variables. Of particular relevance is that – in contrast to the variance – the metric variance Mvar of a compositional distribution is therefore unbounded, which simplifies the selection of α and β (see Choosing beta distribution parameters in the Methods).

Of course, we not only want the $\hat{q}_A$ to be valid PPFs, but also descriptive of the model and data. We express this wish with two additional constraints, which together define a notion of closeness to q_A^*:

- At each intermediate point $\Phi \in (0, 1)$, the *centre* is given by $q_A^*(\Phi)$:

$$\mathbb{E}_a[\hat{q}(\Phi)] = q_A^*(\Phi)\,. \tag{20}$$

- At each intermediate point $\Phi \in (0, 1)$, the *metric variance* is proportional to the square of $\delta_A^{\mathrm{EMD}}(\Phi)$:

$$\mathrm{Mvar}[\hat{q}(\Phi)] = c\,\delta_A^{\mathrm{EMD}}(\Phi)^2\,, \tag{21}$$

where $c > 0$ is the aforementioned sensitivity parameter (also further described in the section on calibration below).

In addition, for reasons of convenience, we also ask that

- The end points are sampled from Gaussian distributions:

$$\begin{aligned}\hat{q}(0) &\sim \mathcal{N}(q^*_A(0), c\,\delta^{\text{EMD}}_A(0)^2)\,,\\ \hat{q}(1) &\sim \mathcal{N}(q^*_A(1), c\,\delta^{\text{EMD}}_A(1)^2)\,.\end{aligned} \tag{22}$$

Thus the process $\mathfrak{Q}_{A;c}$ should be parameterized by two functions and a scalar: q^*_A, δ^{EMD}_A and c. It should be molded to produce realizations $\hat{q}$ which as a whole track q^*_A, with more variability between realizations at points Φ where $\delta^{\text{EMD}}_A(\Phi)$ is larger. This tracking however may be imperfect, because we must also satisfy the constraints of monotonicity and reversibility.

To the best of our knowledge the current literature does not provide a process satisfying all of these constraints. To remedy this situation, we propose a new *hierarchical beta (HB) process*, which we illustrate in Fig. 6. A few example realizations of $\hat{q} \sim \mathfrak{Q}_A$ are drawn as grey lines in Fig. 6**a**. The mixed PPF q^*_A (equation (20)) is drawn as a green line, while the region corresponding to $q^*_A(\Phi) \pm \sqrt{c}\delta^{\text{EMD}}_A(\Phi)$ is shaded in yellow.

Figure 6 shows distributions of $\hat{q}(\Phi)$ at three different values of Φ. The value of $q^*_A(\Phi)$ is indicated by the green vertical bar and agrees well with $\mathbb{E}_a[\hat{q}(\Phi)]$; the desideratum of equation (20) is therefore satisfied. The scaling of these distributions with δ^{EMD}_A (equation (21)) is however only approximate, which we can see as the yellow shading not having the same width in each panel. This is a result of the tension with the other constraints: the HB process ensures that the monotonicity and integrability constraints are satisfied exactly, but allows deviations in the statistical constraints.

A realization of an HB process is obtained by a sequence of refinements; we illustrate three such refinements steps in the rightmost column of Fig. 6. The basic idea is to refine an increment $\Delta\hat{q}_{\Delta\Phi}(\Phi) := \hat{q}(\Phi+\Delta\Phi) - \hat{q}(\Phi)$ into two subincrements $\Delta\hat{q}_{\frac{\Delta\Phi}{2}}(\Phi)$ and $\Delta\hat{q}_{\frac{\Delta\Phi}{2}}(\Phi+\frac{\Delta\Phi}{2})$, with $\Delta\hat{q}_{\frac{\Delta\Phi}{2}}(\Phi)+\Delta\hat{q}_{\frac{\Delta\Phi}{2}}(\Phi+\frac{\Delta\Phi}{2}) = \Delta\hat{q}_{\Delta\Phi}(\Phi)$. To do this, we first determine appropriate parameters α and β, draw x_1 from the corresponding beta distribution and assign

$$\begin{aligned}\Delta\hat{q}_{\frac{\Delta\Phi}{2}}(\Phi) &\leftarrow x_1\Delta\hat{q}_{\Delta\Phi}(\Phi)\,,\\ \Delta\hat{q}_{\frac{\Delta\Phi}{2}}(\Phi+\tfrac{\Delta\Phi}{2}) &\leftarrow x_2\Delta\hat{q}_{\Delta\Phi}(\Phi)\,,\end{aligned} \tag{23}$$

where again $x_2 = (1 - x_1)$. Figure 6c shows distributions for the first (orange) and second (blue) subincrements at the fourth refinement step, where we divide an increment over an interval of length $\Delta\Phi = 2^{-3}$ to two subincrements over intervals of length 2^{-4}. Each pair of subincrements is drawn for a different distribution, which depends on the particular realization $\hat{q}$, but we can nevertheless see the PPF reflected in the aggregate distribution: the PPF has positive curvature, so the second subincrement tends to be larger than the first. Also both increments are bounded from below by 0, to ensure monotonicity.

A complete description of the HB process, including a procedure for choosing the beta parameters α and β such that our desiderata are satisfied, is given in the Methods.

2.5.2 *Using $\mathfrak{Q}$ to compare models*

Having constructed a process $\mathfrak{Q}_{A;c}$ for a candidate model $\mathcal{M}_A$, we can use it to induce a distribution on risks. We do this by generating a sequence of PPFs $\hat{q}_{A,1}, \hat{q}_{A,2}, \ldots, \hat{q}_{A,M_A}$, where $M_A \in \mathbb{N}$ and each $\hat{q}_{A,i}$ is drawn from $\mathfrak{Q}_{A;c}$ (see Fig. 6 for examples of sampled $\hat{q}_{A,i}$, and the Methods for more details on how we evaluate B^{EMD}). As we explain in the next section, the sensitivity parameter c is a property of the experiment (and therefore of the dataset); it is the same for all candidate models.

For each generated PPF, we evaluate the risk functional (using the integral form of equation (14)), thus obtaining a sequence of scalars $R[\hat{q}_{A,1}], R[\hat{q}_{A,2}], \ldots, R[\hat{q}_{A,M_A}]$ which follows $p(R_A \mid \mathfrak{Q}_A)$. With M_A sufficiently large, these samples accurately characterize the distribution $p(R_A \mid \mathfrak{Q}_A)$ (we use $\leftrightarrow$ to relate equivalent descriptions):

$$\begin{aligned}R_A \sim\; & p(R_A \mid \mathcal{D}_{\text{test}}, \mathcal{M}_A; c)\\ &\leftrightarrow \left\{R[\hat{q}_{A,1}], R[\hat{q}_{A,2}], \ldots, R[\hat{q}_{A,M_A}] \;\middle|\; \hat{q}_A \sim \mathfrak{Q}_A\right\}.\\ &\leftrightarrow \left\{R_{A,1}\,,\;\; R_{A,2}\,,\;\; \ldots, R_{A,M_A}\right\}.\end{aligned} \tag{24}$$

Repeating this procedure for a different model $\mathcal{M}_B$ yields a different distribution for the risk:

$$R_B \sim p(R_B \mid \mathcal{D}_{\text{test}}, \mathcal{M}_B; c) \;\leftrightarrow\; \left\{R_{B,1}\,, R_{B,2}\,, \ldots, R_{B,M_B}\right\}. \tag{25}$$

The $B^{\text{EMD}}_{AB;c}$ criterion (10) then reduces to a double sum:

$$\begin{aligned}B^{\text{EMD}}_{AB;c} &:= P(R_A < R_B \mid c)\\ &\approx \frac{1}{M_A M_B}\sum_{i=1}^{M_A}\sum_{j=1}^{M_B}\mathbf{1}_{R_{A,i}<R_{B,j}}\,.\end{aligned} \tag{26}$$

In equation (26), the term within the sum is one when $R_{A,i} < R_{B,j}$ and zero otherwise. A value of $B^{\text{EMD}}_{AB;c}$ greater (less) than 0.5 indicates evidence for (against) model $\mathcal{M}_A$.

We view the undetermined parameter c as a way to adjust the sensitivity of the criterion: larger values of c will typically lead to broader distributions of R_A, and therefore lead to a more conservative criterion (i.e. one which is more likely to result in an equivocal outcome). We give some guidelines on choosing c as part of the calibration procedure described below.

2.6 Calibrating and validating the B^{EMD}

In a previous section we defined the mismatch δ^{EMD}_A between some observed data $\mathcal{D}_{\text{test}}$ and a candidate model $\mathcal{M}_A$ to quantify a lower bound on the epistemic uncertainty of that model. We then proceeded to list desiderata for a process $\mathfrak{Q}$ which converts that uncertainty into a distribution over risks. However, the validation of our approach has remained anecdotal, consisting mainly of observing that the resulting R-distributions look as we expect (Fig. 3).

To put the B^{EMD} criterion on firmer footing, recall that when we linked generalisability, reproducibility and robustness, we motivated distributions on the risk as a way to express epistemic

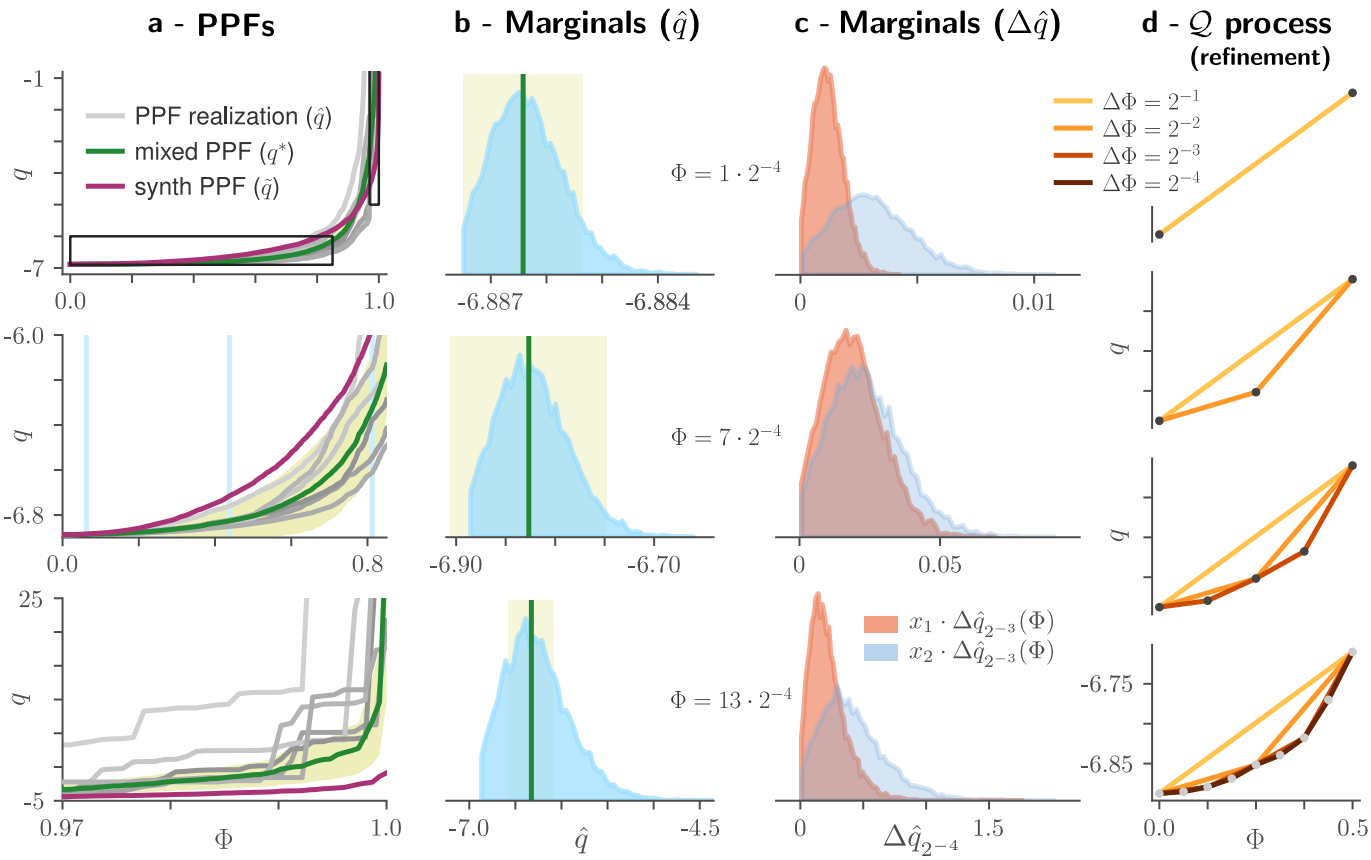

Figure 6: **Sampling a hierarchical beta (HB) process.** **(a)** PPF samples (grey lines) drawn from a hierarchical process $\mathfrak{Q}$. Mixed (green) and synthetic (red) PPFs are those for the Planck model of Fig. 8f (respectively q^* from equation (13) and $\tilde{q}$ from equation (16)). Lower panels are enlarged portions of the top panel, corresponding to the black rectangles in the latter. At each Φ, the variance between realizations is controlled by $\sqrt{c}\,\delta^{\mathrm{EMD}}$ (yellow shading), per equation (21); here we use $c = 0.5$. **(b)** Marginals of $\mathfrak{Q}$ at three values of Φ, obtained as histograms of 10,000 realizations $\hat{q}$. As in (a), the green line indicates the value of $q^*(\Phi)$ and the yellow shading describes the range $q^*(\Phi) \pm \sqrt{c}\delta^{\mathrm{EMD}}(\Phi)$. Values of Φ are given alongside the panels and drawn as cyan vertical lines in (a). **(c)** Distributions of the subincrements drawn at the same three Φ positions as in (b), obtained as histograms from the same 10,000 realizations. Subincrements are for the fourth refinement step, corresponding to the fourth panel of (d). Notation in the legend corresponds to equation (23). **(d)** Illustration of the refinement process. This $\mathfrak{Q}$ is parameterized by the same PPFs as the one in (a–c), but we used a larger c (16) to facilitate visualization. Each refinement step halves the width $\Delta\Phi$ of an increment; here we show four refinements steps, while in most calculations we use eight.

uncertainty; we also gave an explicit example of an *epistemic distribution* Ω (equation (9)) representing variations in an experiment. To calibrate the $B^{\text{EMD}}_{AB;c}$, we can define a set of simulated experiments where we know the true data-generating process $\mathcal{M}_{\text{true}}$ and can therefore define an epistemic distribution Ω. We then define an alternative criterion, (see the Methods for details)

$$B^{\text{epis}}_{AB;\Omega} := P(R_A < R_B \mid \Omega)\,, \tag{27}$$

using the epistemic distribution Ω instead of the process $\mathfrak{Q}_A$ to represent epistemic uncertainty. We then look for $c > 0$ such that the criterion $B^{\text{EMD}}_{AB;c}$ a) is correlated with $B^{\text{epis}}_{AB;\Omega}$; and b) satisfies

$$\left|B^{\text{EMD}}_{AB;c} - 0.5\right| \leq \left|B^{\text{epis}}_{AB;\Omega} - 0.5\right|. \tag{28}$$

Equation (28) says that the criterion $B^{\text{EMD}}_{AB;c}$ should not be overconfident (recall equation (8)).

Note that $B^{\text{epis}}_{AB;\Omega}$ has a clear interpretation: a value near 1 (0) indicates that the selection of model $\mathcal{M}_A$ ($\mathcal{M}_B$) is robust against the variations described by Ω. However it can only be computed for simulated experiments where we can parameterize $\mathcal{M}_{\text{true}}$, since we need to average the comparison outcome over many datasets. On the other hand, although the ontological interpretation of $B^{\text{EMD}}_{AB;c}$ is less clear, its computation requires only samples from $\mathcal{M}_{\text{true}}$ – the model itself can be unknown. *By choosing c such that the criteria are correlated, we transfer the interpretability of* $B^{\text{epis}}_{AB;\Omega}$ *onto* $B^{\text{EMD}}_{AB;c}$. Moreover, if we can find such a c, then we have de facto validated $B^{\text{EMD}}_{AB;c}$ for the set of simulated experiments described by Ω.

Since defining an epistemic distribution involves making many arbitrary choices, one may want to define multiple distributions $\Omega_1, \Omega_2, \ldots$ to ensure that results are not sensitive to a particular choice of Ω. Equation (28) can easily be generalised to account for this, in which case it becomes

$$\left|B^{\text{EMD}}_{AB;c} - 0.5\right| \leq \min_{\Omega \in \{\Omega_1, \Omega_2, \ldots\}} \left|B^{\text{epis}}_{AB;\Omega} - 0.5\right|. \tag{29}$$

We found that an effective way to verify equation (28) is by plotting $B^{\text{epis}}_{AB;\Omega}$ against $B^{\text{EMD}}_{AB;c}$, where values of $B^{\text{epis}}_{AB;\Omega}$ are obtained by averaging comparison outcomes, conditioned on the value of $B^{\text{EMD}}_{AB;c}$ being within an interval. We thus obtain a histogram of $B^{\text{epis}}_{AB;\Omega}$ against $B^{\text{EMD}}_{AB;c}$, which works best when the size of bins is adjusted so that they have similar statistical power. We illustrate this in Fig. 7, where histograms are shown as curves to facilitate interpretation. These curves are drawn against the "overconfident regions" (where equation (28) is violated), depicted in red or yellow: therefore we look for values of c which as much as possible stay within the white regions. The visual representation makes it easier to judge the extent to which small violations of equation (28) can be tolerated.

Figure 7 shows calibration curves for six different epistemic distributions: three model pairs ($\mathcal{M}_A$ vs $\mathcal{M}_B$, $\mathcal{M}_C$ vs $\mathcal{M}_D$, and $\mathcal{M}_A$ vs $\mathcal{M}_D$), each with `weak` and `strong` external input I_{ext}. (For full details on the choice of epistemic distribution, see the Methods.) The model pairs were chosen to test three different situations: one where the candidate models are similar both to each other and the observations ($\mathcal{M}_A$ vs $\mathcal{M}_B$), one where the candidate models are similar to each other but different from the observations ($\mathcal{M}_C$ vs $\mathcal{M}_D$), and one where only one of the candidates is similar to the observations ($\mathcal{M}_A$ vs $\mathcal{M}_D$). For low to moderate c, we see that B^{epis} strongly correlates with B^{EMD}, which confirms that $B^{\text{EMD}}_{ab;c}$ can be an estimator for the probability $P(R_a < R_b)$ (recall equations (10) and (27)). In this case we chose the value $c = 2^{-2}$ since it avoids the overconfidence (red and yellow) regions under most conditions.

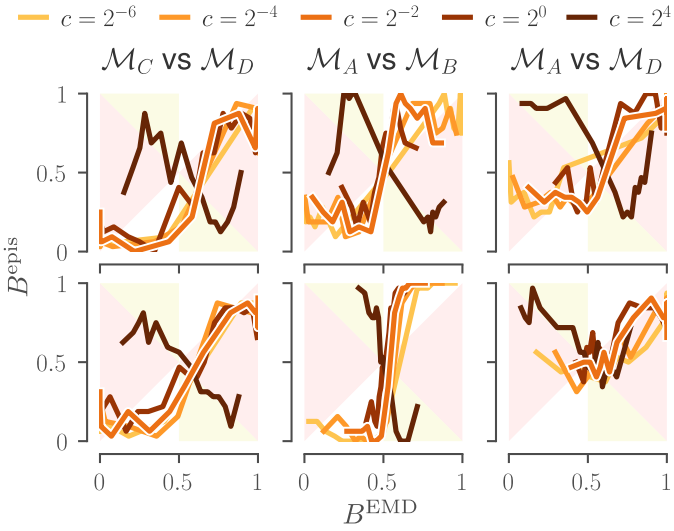

Figure 7: **Calibration curves for the LP models of Fig. 2.** Calibration curves for six epistemic distributions, computed following our proposed calibration procedure. Each curve summarizes 512 simulated experiments with datasets of size 4000, and the six panels explore how curves depend on three parameters: the pair of models being compared, the constant c and the input strength I_{ext}. The latter is either `weak` **(top)** or `strong` **(bottom)**. Other parameters are kept fixed, namely a `short` correlation time τ and a `Gaussian` observation noise with `low` standard deviation. (For an extended version where all conditions are tested, see Supplementary Fig. 1.) The regions depicted in red and yellow are those where equation (28) is violated.

It is worth noting that this calibration procedure works best between similar models: we want to probe the full range of possible values for B^{EMD} and B^{epis}, both of which take values in $(0, 1)$. In particular this requires that for a subset of the simulated experiments, the risk should be similar under both models.

Also worth noting is that there is an upper limit to the value we can choose for c, as evidenced by the curves reversing in Fig. 7 when we set $c = 2^4$. This can be understood as the monotonicity constraint placing an upper bound on the achievable metric variance of $\mathfrak{Q}$.

2.7 Characterizing the behaviour of R-distributions

To better anchor the interpretability of R-distributions, in this section we perform a more systematic study of the relationship between epistemic uncertainty, aleatoric uncertainty, and the shape of the R-distributions. To do this we use a different example, chosen for its illustrative simplicity, which allows us to independently adjust the ambiguity (how much two models are qualitatively similar) and the level of observation noise.

Concretely, we imagine a fictitious historical scenario where the Rayleigh-Jeans

$$\mathcal{B}_{\mathrm{RJ}}(\lambda; T) = \frac{2ck_BT}{\lambda^4} \tag{30}$$

and Planck

$$\mathcal{B}_{\mathrm{P}}(\lambda; T) = \frac{2hc^2}{\lambda^5} \frac{1}{\exp\left(\frac{hc}{\lambda k_B T}\right) - 1} \tag{31}$$

models for the radiance of a black body are two candidate models given equal weight in the scientific community. They stem from different theories of statistical physics, but both agree with observations at infrared or longer wavelengths, and so both are plausible if observations are limited to that window. (When it is extended to shorter wavelengths, the predictions diverge and it becomes clear that the Planck model is the correct one.)

Remark For our purposes, these are just two models describing the relationship between an independent variable λ (the wavelength) and a dependent variable $\mathcal{B}$ (the spectral radiance), given a parameter T (the temperature) which is inferred from data; our discussion is agnostic to the underlying physics. The parameters h, c and k_B are known physical constants (the Planck constant, the speed of light and the Boltzmann constant) and can be omitted from the discussion.

We use a simple Poisson counting process to model the data-generating model $\mathcal{M}_{\mathrm{true}}$ including the observation noise:

$$\mathcal{B} \mid \lambda, T, s \sim \frac{1}{s} \mathrm{Poisson}(s\, \mathcal{B}_{\mathrm{P}}(\lambda; T)) + \mathcal{B}_0\,, \tag{32}$$

where s is a parameter related to the gain of the detector (see the Methods for details). Most relevant to the subsequent discussion is that the mean and variance of $\mathcal{B}$ are

$$\mathbb{E}[\mathcal{B}] = \mathcal{B}_{\mathrm{P}}(\lambda; T) + \mathcal{B}_0\,,$$
$$\mathbb{V}[\mathcal{B}] = \frac{\mathcal{B}_{\mathrm{P}}(\lambda; T)}{s}\,,$$

and can therefore be independently controlled with the parameters $\mathcal{B}_0$ and s.

For the purposes of this example, both *candidate* models $\mathcal{M}_{\mathrm{RJ}}$ and $\mathcal{M}_{\mathrm{P}}$ make the incorrect (but common) assumption of additive Gaussian noise, such that instead of equation (32) they assume

$$\mathcal{B} \mid \lambda, T, \sigma \sim \mathcal{N}(\mathcal{B}_a(\lambda; T), \sigma^2)\,, \tag{33}$$

with $\mathcal{B}_a \in \{\mathcal{B}_{\mathrm{RJ}}, \mathcal{B}_{\mathrm{P}}\}$ and $\sigma > 0$. This ensures that there is always some amount of mismatch between $\mathcal{M}_{\mathrm{true}}$ and the two candidates. That mismatch is increased when $\mathcal{B}_0 > 0$, which we interpret as a sensor bias which the candidate models neglect.

With this setup, we have four parameters which move the problem along three different "axes": The parameters λ_{min} and λ_{max} determine the spectrometer's detection window, and thereby the **ambiguity**: the shorter the wavelength, the easier it is to distinguish the two models. The parameter s determines the **level of noise**. The parameter $\mathcal{B}_0$ determines an additional amount of **model mismatch** between the candidate model and the data.

We explore these three axes in Fig. 8, and illustrate how the overlap of the R_{P} and R_{RJ} distributions changes through mainly two mechanisms: Better data can shift one R-distribution more than the other, and/or it can tighten one or both of the R-distributions. Either of these effects can increase the separability of the two distributions (and therefore the strength of the evidence for falsifying one of them).

2.8 The B^{EMD} avoids the overconfidence of other model selection criteria

A guiding principle in developing the B^{EMD} criterion was to address the tendency of model selection criteria to be overconfident. To show how it fares in comparison with other established criteria, we generated 18 variations of datasets generated with equation (32): three levels of noise s (ranging from high, 2^{12}, to low 2^{20} [$\mathrm{m}^2 \cdot \mathrm{nm} \cdot \mathrm{photons} \cdot \mathrm{sr} \cdot \mathrm{kW}^{-1}$]), three dataset sizes L (2^9, 2^{12}, and 2^{15}) and two wavelength ranges (20–1000 μm and 15–30 μm). Datasets with high noise and long wavelengths provide almost no discriminatory information: the two model predictions are almost the same, and any discrepancy between them is dwarfed by the amount of noise. At the other end, the low noise, short wavelength datasets are at the threshold between moderate and strong evidence in favour of $\mathcal{M}_{\mathrm{P}}$. We avoid going as low as the visible range: there the evidence is so decisive that the problem stops being interesting.

Our results are summarised in Table 2, for which it helps to keep in mind two signs of overconfidence:

Lack of saturation There should always come a point where enough data have been collected, and simply enlarging the dataset with samples from the same distribution does not provide more information. If a criterion continues increasing or decreasing without bound, then it must be overconfident. (This is akin to the probability of the "equivocal" outcome of equation (7) becoming zero.) In the table therefore we want values to converge as we increase L.

Non-robustness We defined overconfidence as the tendency of a criterion to report strong evidence when its selection outcome is not robust; i.e. the tendency to violate equation (8). Therefore in the table we want large values (those with visible shading) to be *robust*. Values which flip from strong negative to strong positive for small changes of the dataset are overconfident.

In addition to the B^{EMD} and the risk (B^R), Table 2 includes criteria based on the *likelihood ratio* (B^l), the *Bayes factor* (B^{Bayes}) [20, 32] and the *expected log predictive density* (elpd) (B^{elpd}) [19, 20]. Moreover, because $\mathcal{M}_{\mathrm{P}}$ and $\mathcal{M}_{\mathrm{RJ}}$ have the same number of parameters, the likelihood ratio is also equivalent to the *Akaike Information Criterion* (AIC), up to a factor of 2 [20]. Similarly, the two common Bayesian methods of *cross-validation* and *widely applicable information criterion* (WAIC) are approximations of the elpd [19]; they are therefore represented in this table by B^{elpd}.

To allow for comparability, we give each criterion B^C_{AB} as a log probability ratio; i.e. "model A is B^C_{AB} times more probable than model B." Conceptually, if $P(A)$ is the "probability of model A" and $P(B)$ the "probability of model B", then a criterion corres-

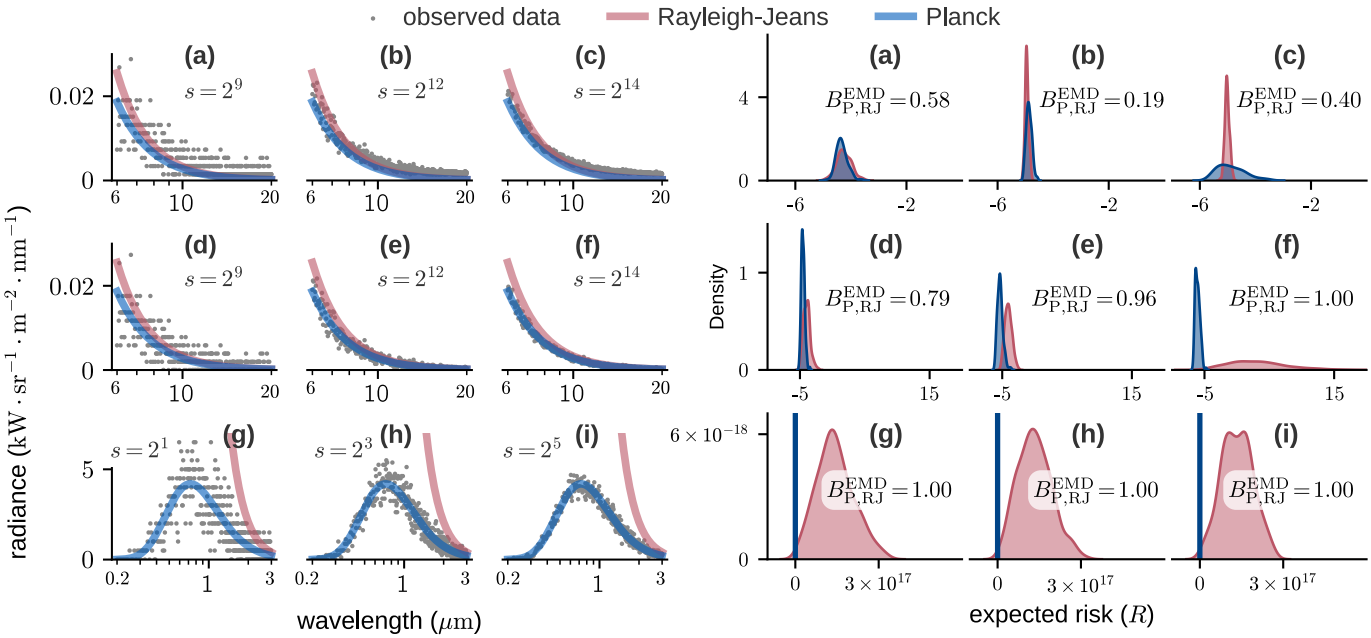

Figure 8: ***R*-distributions** (right) **for different simulated datasets of spectral radiance** (left). Datasets were generated using equation (32). For each model a, the R_a-distribution was obtained by sampling an HB process $\mathfrak{Q}$ parametrized by δ_a^{EMD}; see the respective Results sections for definitions of $\mathfrak{Q}$ and δ^{EMD}. A kernel density estimate is used to visualise the resulting samples (equation (24)) as densities. In all rows, noise (s) decreases left to right. **Top row:** over a range of long wavelengths with positive bias $\mathcal{B}_0 = 0.0015$, both models fit the data equally well. **Middle row:** same noise levels as the first row, but now the bias is zero. Planck model seems to fit better. **Bottom row:** at visible wavelengths, the better fit of the Planck model is incontrovertible. Wavelength ranges are different from those of Table 2 to improve the visualization.

ponds to

$$B^C_{AB} = \frac{P(A)}{P(B)} \quad \leftrightarrow \quad \log_{10} B^C_{AB} = \log_{10} P(A) - \log_{10} P(B)\,. \tag{34}$$

This is the typical form for Bayes' factors, and we use Jeffreys' scale [32, 33] to interpret values in the Table 2: values near 0, ±1 and ±2 respectively correspond to inconclusive, weak, and strong evidence. However this is an approximation since the B^{EMD}, the risk and the AIC are not probability ratios, and we thus needed to stretch some definitions to put them in this form. In particular, for the first two we used the "underbar" quantities

$$\log_{10} \underline{B}^{\mathrm{EMD}}_{AB;c} := \log_{10} B^{\mathrm{EMD}}_{AB;c} - \log_{10}(1 - B^{\mathrm{EMD}}_{AB;c})\,, \tag{35}$$

$$\log_{10} \underline{B}^{R}_{AB} := -R_A + R_B \;/\; \log 10\,. \tag{36}$$

Values of $\underline{B}^{\mathrm{EMD}}_{AB;c}$ and $\underline{B}^{R}_{AB}$ are therefore not directly comparable with those of $B^{\mathrm{EMD}}_{AB;c}$ and B^{R}_{AB} reported elsewhere in this paper. In Table 2, the $\log_{10} \underline{B}^{\mathrm{EMD}}_{AB;c}$ ranges from $-\infty$ to ∞, with values $\pm\infty$ indicating that the two R-distributions have zero overlap.

The expressions used to compute the other criteria are listed in Section 4.7. Computing the Bayesian criteria also requires priors for σ and T; we used log uniform priors with $\sigma \in [2^9, 2^{14}]$ and $T \in [1000, 5000]$. Calculations were also repeated with priors with much tighter bounds and yielded similar values.

Inspection of Table 2 reveals a few important features. First we notice that the naive likelihood ratio (B^l) is an especially bad criterion: it does not converge as L grows, flips its preference between $\mathcal{B}_{\mathrm{P}}$ and $\mathcal{B}_{\mathrm{RJ}}$ and suggests enormously strong evidence even in cases where the data are ambiguous. For example, we have $B^l = -3.02$ for $\mathcal{B}_0 > 0$ and 35% noise, but then $B^l = +10.33$ when the noise reduces to 9%. Part of these effects are due to the propensity of the likelihood to "stretch" [9, 34] with the number of data points.

As noted below equation (7), the risk criterion B^R is effectively binary: only its sign matters. While we can define $\underline{B}^{R}_{AB}$ to take real values, as we did here, those values do not allow to predict the robustness of the criterion. This is a problem, because without a way to quantify robustness, we have no basis for discarding the negative values which seem to favour the Rayleigh-Jeans model.

The two Bayesian criteria (B^{Bayes} and B^{elpd}) are notable by their extremely small values, which may suggest that they are excessively conservative. Despite this, they also do not saturate with L: the probabilistic ratios may be valid in their strict Bayesian definition, but since that definition is sensitive to L, their practical usefulness for experimental data is diminished. Bayes factors in addition are highly sensitive to modelling choices which should be irrelevant, such as the scale of a noninformative prior [16], which makes their use for model selection haphazard at best. The Bayesian criteria are also by far the most computationally expensive of the criteria studied in Table 2.

If we are to interpret the values of criteria as relative probabilities, the global pattern we would expect to see in Table 2 is that cells become progressively more blue as we go to the right (less noise, less model mismatch) and as we go down (more data, less ambiguous data). Only the B^{EMD} follows this pattern, suggesting that interpreting it as advertised – as the probability $P(R_A < R_B)$ – is sound.

3 Discussion

Our approach to model selection views the selection outcome as the result of an experiment. In this view, and in line with recent works [23, 24], we therefore argued that a model selection procedure must be *reproducible* across experimental conditions, in order for the selection result to *generalise* beyond the laboratory. Mathematically, this is expressed as *robustness* of the selection outcome vis-à-vis changes of the data distribution of $\mathcal{D}_{\mathrm{test}}$, changes which represent our *epistemic uncertainty*.

We formalized this idea in the form of *R-distributions*, which describe the uncertainty on a model's risk given observed data. When we account for epistemic uncertainty, R-distributions do not become degenerate but maintain a finite width – even in the limit of infinite data. To estimate them, we considered the mimimum epistemic uncertainty required to account for the mismatch between model predictions and actual data. This we quantified as the *empirical model discrepancy* (δ^{EMD}; the difference between two PPFs of the loss), from which we defined a stochastic process $\mathfrak{Q}$ which allows to sample values of the risk R. A big advantage of working with PPFs of the loss is that they are always one-dimensional. As a consequence, the stochastic process $\mathfrak{Q}$ is relatively stereotyped – in fact, many of the calculation steps visually summarized in Fig. 1 can be automated (see Code availability).

The comparison of two R-distributions for candidate models $\mathcal{M}_A$ and $\mathcal{M}_B$ is then a simple probability, $P(R_A < R_B)$, which is how we ultimately define the EMD criterion B^{EMD}_{AB}. This provides a clear interpretation of the falsification threshold ϵ: if $B^{\mathrm{EMD}}_{AB} \geq \epsilon = 0.95$, then in at least 95 % of replications (i.e. variations of $\mathcal{D}_{\mathrm{test}}$), experiments should find that model $\mathcal{M}_A$ fits the data better than model $\mathcal{M}_B$ (in the sense of having lower empirical risk). Guidelines for choosing falsification thresholds should therefore be similar to those for choosing significance levels, and as long as this value is greater than the reciprocal golden ratio, comparisons between models will be transitive (equation (11)).

We illustrated the approach on two example problems, one describing the radiation spectrum of a black body, and the other the dynamical response of a neuron of the lobster pyloric circuit. In the case of the former, we compared the Planck and Rayleigh-Jeans models – two structurally different models, which are therefore also amenable to comparison with other established criteria (Table 2). While some of the other criteria consistently identified the correct model, only the B^{EMD} had magnitudes which could be usefully interpreted as a degree of certainty. The simplicity of the black body radiation models also allowed us to systematically characterize how model ambiguity, observation noise, and data–model mismatch affects the R-distributions (Fig. 8).

The neural dynamics example was inspired by the increasingly common practice of data-driven modelling. Indeed, Prinz *et al.* [6, 35] – whose work served as the basis for this example – can be viewed as early advocates for data-driven approaches. Although their exhaustive search strategy faces important limitations [36], more recent approaches are much more scalable. For

Table 2: **Comparison of different model selection criteria** for variations of the datasets shown in Fig. 8. Criteria compare the Planck model ($\mathcal{M}_\mathrm{P}$) against the Rayleigh-Jeans model ($\mathcal{M}_\mathrm{RJ}$) and are evaluated for different dataset sizes (L), different levels of noise (s) and different wavelength windows (λ). To allow for comparisons, all criteria have been transformed into ratios of probabilities (see equations (35) and (36)). **Values reported are the** $\log_{10}$ **of those ratios.** Positive (blue shaded) values indicate evidence in favour of the Planck model, while negative (red shaded) values indicate the converse. For example, a value of +1 is interpreted as $\mathcal{M}_\mathrm{P}$ being 10 times more likely than $\mathcal{M}_\mathrm{RJ}$, while a value of -2 would suggest that $\mathcal{M}_\mathrm{P}$ is 100 times *less* likely than $\mathcal{M}_\mathrm{RJ}$. Noise levels are reported in two ways: s is the actual value used to generate the data, while "rel. σ" reports the resulting standard deviation as a fraction of the maximum radiance within the data window. The 20–1000 µm window for λ stretches into the far infrared range, where the two models are nearly indistinguishable; hence higher positive values are expected for zero bias, low noise, and the 15–30 µm window. As in Fig. 8, calculations were done for both positive and null bias conditions (resp. ($\mathcal{B}_0 > 0$ and $\mathcal{B}_0 = 0$); the former emulates a situation where neither model can fit the data perfectly. Expressions for all criteria are given in Section 4.7. For the $\underline{B}^{\mathrm{EMD}}_{\mathrm{P,RJ}}$ criteria, we used $c = 0.5$. Although this is the same value as we used for neuron model, it was determined through a separate calibration with different epistemic distributions.

			$\mathcal{B}_0 > 0$			$\mathcal{B}_0 = 0$		
		s	2^{12}	2^{16}	2^{20}	2^{12}	2^{16}	2^{20}
		rel. σ	35%	9%	2%	36%	9%	2%
Criterion	$\lambda(\mu\mathrm{m})$	L						
$\underline{B}^{\mathrm{EMD}}_{\mathrm{P,RJ}}$	20–1000	512	−0.05	0.13	0.33	−0.15	0.16	0.34
		4096	0.01	−0.02	0.36	-7×10^{-3}	0.02	0.47
		32768	−0.08	−0.02	0.24	−0.06	−0.11	0.40
	15–30	512	0.05	0.49	∞	-4×10^{-3}	0.35	∞
		4096	0.05	0.45	2.27	−0.03	0.49	2.62
		32768	−0.13	0.36	3.13	0.06	0.26	∞
$\underline{B}^{R}_{\mathrm{P,RJ}}$	20–1000	512	2×10^{-5}	-5×10^{-4}	5×10^{-3}	2×10^{-5}	-7×10^{-4}	4×10^{-3}
		4096	2×10^{-5}	-5×10^{-4}	5×10^{-3}	2×10^{-5}	-7×10^{-4}	4×10^{-3}
		32768	2×10^{-5}	-5×10^{-4}	5×10^{-3}	2×10^{-5}	-7×10^{-4}	4×10^{-3}
	15–30	512	8×10^{-5}	6×10^{-4}	0.01	8×10^{-5}	6×10^{-4}	9×10^{-3}
		4096	8×10^{-5}	6×10^{-4}	0.01	8×10^{-5}	6×10^{-4}	9×10^{-3}
		32768	8×10^{-5}	6×10^{-4}	0.01	8×10^{-5}	6×10^{-4}	9×10^{-3}
$B^{l}_{\mathrm{P,RJ}}$	20–1000	512	−0.72	−0.74	5.64	−0.72	−0.82	4.62
		4096	0.64	−0.41	14.49	0.62	−1.05	7.94
		32768	−3.02	10.33	40.41	−3.23	8.11	−8.50
	15–30	512	0.06	−0.35	3.27	0.06	−0.39	2.61
		4096	0.52	3.86	52.20	0.49	3.53	47.12
		32768	3.04	23.02	389.62	2.87	20.33	348.85
$B^{\mathrm{Bayes}}_{\mathrm{P,RJ};\pi}$	20–1000	512	3×10^{-12}	3×10^{-12}	3×10^{-12}	3×10^{-12}	3×10^{-12}	3×10^{-12}
		4096	4×10^{-11}	5×10^{-11}	4×10^{-11}	4×10^{-11}	4×10^{-11}	5×10^{-11}
		32768	4×10^{-10}	4×10^{-10}	4×10^{-10}	4×10^{-10}	4×10^{-10}	4×10^{-10}
	15–30	512	1×10^{-9}	1×10^{-9}	1×10^{-9}	1×10^{-9}	1×10^{-9}	1×10^{-9}
		4096	3×10^{-8}	3×10^{-8}	3×10^{-8}	3×10^{-8}	3×10^{-8}	3×10^{-8}
		32768	2×10^{-7}	2×10^{-7}	2×10^{-7}	2×10^{-7}	2×10^{-7}	2×10^{-7}
$B^{\mathrm{elpd}}_{\mathrm{P,RJ};\pi}$	20–1000	512	0	0	0	0	0	0
		4096	0	0	0	0	0	0
		32768	0	0	0	0	0	0
	15–30	512	7×10^{-7}	6×10^{-7}	6×10^{-7}	7×10^{-7}	6×10^{-7}	6×10^{-7}
		4096	5×10^{-6}	5×10^{-6}	5×10^{-6}	5×10^{-6}	5×10^{-6}	5×10^{-6}
		32768	4×10^{-5}	4×10^{-5}	4×10^{-5}	4×10^{-5}	4×10^{-5}	4×10^{-5}

example, methods using gradient based optimization can simultaneously learn dozens – or in the case of neural networks, millions – of parameters [2, 37]. These methods however are generally used to solve non-convex problems, and therefore run against the same follow-up question: *having found (possibly many) candidate models, which ones are truly good solutions, and which ones should be discarded as merely local optima?* Our B^{EMD} criterion, which assigns epistemic uncertainty to a model's risk (i.e. its score), can address this latter question. It can do so even when candidate models are structurally identical (distinguished therefore only by the values of their parameters), which sets it apart from other model selection criteria.

A few other model selection methods have been proposed for structurally identical candidate models, either within the framework of approximate Bayesian computing [38] or by training a machine learning model to perform model selection [39]. Largely these approaches extend Bayesian model selection to cases where the model likelihood is intractable, and as such inherit the same challenges as the Bayesian methods we studied in Table 2 (in addition to introducing additional ones). In particular, they make no special treatment for epistemic uncertainty, treating it simply as a prior over models – a strategy which, as more recently noted by Gelman & Yao [16], easily leads to paradoxical results.

Epistemic uncertainty itself is not a novel idea: Kiureghian & Ditlevsen [11] discuss how it should translate into scientific practice, and Hüllermeier & Waegeman [13] do the same for machine learning practice. More specific to model selection, previous efforts to include epistemic uncertainty include the GLUE methodology [8, 34], Bayesian calibration [10, 40], Bayesian neural networks [15], and drop-out regularization at test time [12]. These are mostly ensemble methods with a focus on quantifying the effect of uncertainty on *model predictions*; they improve the estimate of risk, but still do not assign uncertainty to that estimate. In contrast, with our B^{EMD} criterion, we express epistemic uncertainty on the *statistics of the sample loss*. This has two immediate advantages: the method trivially generalises to high-dimensional systems, and we obtain *distributions* for the risk (Fig. 3). It seems reasonable to us that uncertainty in the model should lead to uncertainty in the risk.

We designed the EMD criterion to be compatible with experimental practice. First because our target applications are those involving experimental data, but also because experimental sciences have a long and successful history of selecting models based on their fit to data – including the Eddington observations which inspired Popper's framing of science around *falsification*. In science it is often possible to repeat experiments if the acquired dataset size L is found to be insufficient. It is important therefore that the outcome of a criterion converge as L is increased, a requirement which many standard criteria – including significance tests, information criteria like the AIC, and Bayes factors – fail to meet. Indeed, ensuring convergence in L was a guiding principle for formulating the EMD criterion. Our choice to compare models pairwise is also consistent with Kuhn's [41, Chap. XII] insight that theories (i.e. candidate models) should be falsified not when their fit to data is poor, but when other competing theories fit the data better.

This approach of using conceptually motivated principles to guide the development of a method seems to be fruitful, as it has lead to other recent developments in the field of model inference. For instance, Swigon *et al.* [42] showed that by requiring a model to be invariant under parameter transformation, one can design a prior (i.e. a regularizer) which better predicts aleatoric uncertainty. Another example is simulation-based calibration (SBC) [43, 44], for which the principle is self-consistency of the Bayesian model. This is conceptually similar to the calibration procedure we proposed: in both case a consistency equation is constructed by replacing one real dataset with many simulated ones. The main difference is that SBC checks for consistency with the Bayesian prior (and therefore the aleatoric uncertainty), while we check for consistency with one or more epistemic distributions. In both cases the consistency equation is represented as a histogram: in the case of SBC it should be flat, while in our case it should follow the identity $B^{\text{epis}} = B^{\text{EMD}}$.

The δ^{EMD} discrepancy (equation (17)) also has some similarities with the Kolmogorov-Smirnoff (K-S) statistic; the latter is defined as the difference between two CDFs and is also used to compare models. Methodologically, the K-S statistic is obtained by taking the supremum of the difference, whereas we keep δ^{EMD} as a function over $[0, 1]$; moreover, a Kolmogorov-Smirnoff test is usually computed on the distribution of data samples ($\mathcal{D}_{\text{test}}$) rather than that of their losses ($\{Q(x, y) : (x, y) \in \mathcal{D}_{\text{test}}\}$).

One would naturally expect a comparison criterion to be symmetric: the evidence required to reject model $\mathcal{M}_A$ must be the same whether we compare $\mathcal{M}_A$ to $\mathcal{M}_B$ or $\mathcal{M}_B$ to $\mathcal{M}_A$. Moreover, it must be possible that *neither* model is rejected (what we described as *equivocal* evidence). Bayes factors and information criteria do allow for equivocal statements, but with an important caveat: they provide no principled way to determine the threshold between equivocality and falsification (see our comparison of the B^{EMD} to other criteria). In fact there can be no universal threshold, since it always depends on the dataset size L – in contrast to the B^{EMD} falsification threshold, a Bayes threshold does not converge when the dataset becomes large. Another important consequence of a symmetric criterion is that it trivially generalises to comparing any number of models, such as we did in Table 1.

From a practical standpoint, the most important feature of the B^{EMD} is likely its ability to compare both specific model parameterizations of the same structural model, as well as structurally different models. All other criteria listed in Table 2 only compare model structures, because they either assume globally optimal parameters (likelihood ratio, AIC) or they integrate over the entire parameter space (Bayes factor, elpd). The calculation of the $B^{\text{EMD}}_{AB;c}$ between two models is also reasonably fast, taking less than a minute in most of our examples.

Also important is that computing the B^{EMD} only requires knowledge which is usually accessible in practice: a method to generate synthetic samples from both $\mathcal{M}_A$ and $\mathcal{M}_B$, a method to generate true samples, and a loss function. Some reasoned choices are used to define the stochastic process $\mathfrak{Q}$ in the PPF space, but they are limited by the hard constraints of that space: PPFs must be one-dimensional on $[0, 1]$, monotone, integrable, and non-accumulating. *Hierarchical beta (HB) processes* (which are further detailed in the Methods) satisfy those constraints, but it would be an interesting avenue of research to look for alternatives which also satisfy the desiderata for $\mathfrak{Q}$.

In particular, if one could define processes which better preserve the proportionality of equation (21), or allow for a faster computational implementation, the B^{EMD} could be applied to an even wider range of problems.

To define the discrepancy function δ^{EMD} (17), we assumed datasets to be sufficiently large that aleatoric uncertainty can be neglected. This was primarily to simplify the presentation. Methods of course already exist to estimate aleatoric uncertainty – the bootstrap and synthetic procedures we used in Fig. 4 being two examples – and ideally both aleatoric and epistemic uncertainty would be combined into a single R-distribution. One simple approach could be to convolve the aleatoric and epistemic R-distributions, but we leave it to future research to determine when this is appropriate, or whether a better approach exists.

More generally, we hope that practitioners view the B^{EMD} criterion not as a prescription, but as a framework which can be adapted to their problem. This adaptativity offers many opportunities to incorporate domain expertise: in the choice of the candidate models, the loss function, sensitivity parameter c, falsification threshold ϵ, and epistemic distributions used to validate c. These are clear interpretable choices which help express scientific intent.

4 Methods

4.1 Poisson noise model for black body radiation observations

In equation (32), we used a Poisson counting process to simulate the observation noise for recordings of a black body's radiance. This is a more realistic model than Gaussian noise for this system, while still being simple enough to serve our illustration.

The physical motivation is as follows. We assume that data are recorded with a spectrometer which physically separates photons of different wavelengths and measures their intensity with a CCD array. We further assume for simplicity that wavelengths are integrated in bins of equal width, such that the values of λ are sampled uniformly (the case with non-uniform bins is less concise but otherwise equivalent). We also assume that the device uses a fixed time window to integrate fluxes, such that what it detects are effective photon *counts*. The average number of counts is proportional to the radiance, but also to physical parameters of the sensor (including size, integration window and sensitivity) which we collect into the factor s; the units of s are $\text{m}^2\cdot\text{nm}\cdot\text{photons}\cdot\text{sr}\cdot\text{kW}^{-1}$, such that $s\mathcal{B}_a(\lambda;T)$ is a number of photons. Since the photons are independent, the recorded number of photons will be random and follow a Poisson distribution. This leads to the following model $\mathcal{M}_{\text{true}}$, which we use to generate the data:

$$\mathcal{B} \mid \lambda, T \sim \frac{1}{s}\,\text{Poisson}(s\,\mathcal{B}_{\text{P}}(\lambda;T)) + \mathcal{B}_0\,, \quad \text{(repeated from (33))}$$
$$\lambda \in \{\lambda_{\min}, \lambda_{\min}+\Delta\lambda, \lambda_{\min}+2\Delta\lambda, \ldots, \lambda_{\max}\}\,. \tag{37}$$

Here $\mathcal{B}_0$ captures the effect of dark currents and random photon losses on the radiance measurement. Recall that a random variable k following a distribution Poisson(μ) has probability mass function $P(k) = \frac{\mu^k e^{-\mu}}{k!}$.

Note that we divide by s so that $\mathcal{B}$ also has dimensions of radiance and is comparable with the models $\mathcal{B}_{\text{P}}$ and $\mathcal{B}_{\text{RJ}}$ defined in equations (30) and (31).

4.2 Neuron model

The neuron model used in our Results is the Hodgkin-Huxley-type model of the lobster pyloric rhythm studied by Prinz *et al.* [6]. The specific implementation we used can be obtained from René [45], along with a complete description of all equations and parameters. We summarize the model below and refer the reader to that reference for more details.

For each cell k, the potential across a patch of area A and capacitance C evolves according to the net ionic current through the cell membrane:

$$\frac{C}{A}\frac{dV^k}{dt} = -\underbrace{\sum_{i\,\in\,\text{ion channels}} I_i^k}_{\substack{\text{ion diffusion}\\ \text{through membrane}}} - \underbrace{\sum_{l\,\in\,\text{neurons}} I_s^l}_{\substack{\text{chemical}\\ \text{synapses}}} - \underbrace{\sum_{l\,\in\,\text{neurons}} I_e^{kl}}_{\substack{\text{electrical}\\ \text{synapses}}} - I_{\text{ext}}^k\,, \tag{38}$$

where I_{ext} is an arbitrary external current, the I_i describe ion exchanges between a cell and its environment, and I_s and I_e describe ion exchanges between different cells. The I_{ext} current can be used to represent a current applied by the experimenter, or the inputs from other cells in the network. The voltage $\tilde{V}$ which an experimenter records would then be some corrupted version of V, subject to noise sources which depend on their experiment.

$$\tilde{V}(t) \sim \text{Experimental noise}\Big(V(t)\Big)\,. \tag{39}$$

We generate the external input I_{ext} as a Gaussian coloured noise with autocorrelation:

$$\Big\langle I_{\text{ext}}(t) I_{\text{ext}}(t')\Big\rangle = \sigma_i^2 e^{-(t-t')^2/2\tau^2}\,. \tag{40}$$

We do this using an implementation[46] of the sparse convolution algorithm [47]. We found that in addition to being more realistic, coloured noise also smears the model response in time and thus reduces degeneracies when comparing models.

Each cell in the model has eight currents through ion channels, indexed by i: one Na^+ current, two Ca^{2+} currents, four K^+ currents and one leak current. Each current is modelled as (square brackets indicate functional dependence)

$$I_e^{kl} = g_e(V^k - V^l)\,, \qquad \tau_{m,i}[V^k]\frac{dm}{dt} = m_{\infty,i}[V^k] - m_i^k\,,$$
$$I_i^k = g_i^k\,(m_i^k)^{p_i}\,h_i\,(V^k - E_i)\,, \qquad \tau_{h,i}[V^k]\frac{dh}{dt} = h_{\infty,i}[V^k] - h_i^k\,,$$
$$I_s^{kl} = g_s^{kl}\,s^l\,(V^k - E_s^k)\,, \qquad \tau_s^l[V^l]\frac{ds}{dt} = s_\infty^l[V^l] - s^l\,.$$

These equations are understood as describing currents through permeable channels with maximum conductivity g_i^k (for membrane currents within the same cells) or g_s^{kl} (for synaptic currents between different cells). Conductivities are dynamic: they are governed by the equations for the gating variables m, h and s given above. (Some channels do not have inactivating gates;

Table 3: Neuron circuit model labels

Model symbol	Model components
$\mathcal{M}_{\text{true}}$	$I_{\text{ext}} \to$ AB 3 $\to$ **LP 1** $\to$ Gaussian noise $\to$ digitize
$\mathcal{M}_A$	$I_{\text{ext}} \to$ AB 3 $\to$ **LP 2** $\to$ Gaussian noise
$\mathcal{M}_B$	$I_{\text{ext}} \to$ AB 3 $\to$ **LP 3** $\to$ Gaussian noise
$\mathcal{M}_C$	$I_{\text{ext}} \to$ AB 3 $\to$ **LP 4** $\to$ Gaussian noise
$\mathcal{M}_D$	$I_{\text{ext}} \to$ AB 3 $\to$ **LP 5** $\to$ Gaussian noise

for these, h_i is set to 1.) The fixed points m_∞, h_∞ and s_∞, as well as the time constants τ_m, τ_h and τ_s, are functions of the voltage; the precise shape of these functions is specific to each channel type and can be found in either Prinz *et al.* [6] or René [45].

Following Prinz et al., we treat the functions m_∞, h_∞, s_∞, τ_m, τ_h and τ_s, as well as the electrical conductance g_e and the Nernst (E_i) and synaptic ($E_{s,k}$) reversal potentials, as known fixed quantities. Thus the only free parameters in this model are the maximum conductances g_i^k and g_s^{kl}: the former determine the type of each neuron, while the latter determine the circuit connectivity.

The pyloric circuit model studied by Prinz *et al.* [35] consists of three populations of neurons with eight different ion channels. Biophysically plausible values for the channel and connectivity parameters were determined through separate exhaustive parameter searches by Prinz et al. [6, 35], the results of which were reduced to sixteen qualitatively different parameter solutions: 5 *AB/PD* cells, 5 *LP* cells and 6 *PY* cells. Importantly, these parameter solutions are distinct: interpolating between them does not yield models which reproduce experimental recordings. For purposes of illustration we study the simple two-cell circuit shown in Fig. 2**a**, where an AB cell drives an LP cell. Moreover we assume the parameters of the AB cell to be known, such that we only need to compare model candidates for the LP cell. (These assumptions are not essential to applying our method, but they avoid us contending with model-specific considerations orthogonal to our exposition.)

The AB neuron is an autonomous pacemaker and serves to drive the circuit with realistic inputs; all of our examples use the same AB model (labelled 'AB/PD 3' in Table 2 of Prinz *et al.* [6]), whose output is shown in Fig. 2**b**. Panels **c** and **d** show the corresponding response for each of the five LP models given in Table 2 of Prinz *et al.* [6].

To generate our simulated observations, we use the output of `LP 1`, add Gaussian noise and then round the result (in millivolts) to the nearest 8-bit integer; in this way $\mathcal{M}_{\text{true}}$ includes both electrical and digitization noise. This leaves `LP 2` through `LP 5` to serve as candidate models; for these we assume only Gaussian noise, and we label them $\mathcal{M}_A$ to $\mathcal{M}_D$. We use Θ_a to denote the concatenation of all parameters for a given model a, which here consist of the vectors of conductance values g_i and g_s. Model definitions are summarized in Table 3 and Algorithm 1.

4.3 Loss function for the neuron model

To evaluate the risk of each candidate model, we use the log likelihood of the observations (equation (6)). This standard choice is convenient for exposition purposes: it is simple to explain and illustrates the generality of the method, since a likelihood function is available for any model in the form of equation (1).

However it is not a requirement to use the negative log likelihood as the loss, and in fact for time series models it can be disadvantageous. For example, the neuron models used in this work have sharp temporal responses (spikes), which makes the log likelihood sensitive to the timing of these spikes. In practice a less sensitive loss function may be preferable, although the best choice will depend on the application.

Algorithm 1 Neuron model

procedure GENERATE DATA($\mathcal{T}$)
  for $t \in \mathcal{T}$ **do**
    integrate equation (38) to obtain $V^{\texttt{AB}}(t)$, $V^{\text{LP}}(t; \Theta_{\text{true}})$
    draw $\xi(t) \sim \mathcal{N}(0, \sigma_o)$
    evaluate $\tilde{V}^{\text{LP}}(t) = \texttt{digitize}_8\big(V^{\text{LP}}(t) + \xi(t)\big)$
  end for
  return $\{\, \tilde{V}^{\text{LP}}(t) : t \in \mathcal{T} \,\}$
end procedure

procedure SIMULATE CANDIDATE($\mathcal{T}$, $a \in \{A, B, C, D\}$)
  for $t \in \mathcal{T}$ **do**
    integrate equation (38) to obtain $V^{\texttt{AB}}(t)$, $V^{\text{LP}}(t; \Theta_a)$
    draw $\xi(t) \sim \mathcal{N}(0, \sigma_o)$
    evaluate $\tilde{V}^{\text{LP}}(t) = V^{\text{LP}}(t; \Theta_a) + \xi(t)$.
  end for
  return $\{\, \tilde{V}^{\text{LP}}(t) : t \in \mathcal{T} \,\}$
end procedure

procedure $\texttt{digitize}_8(\text{x})$
Simulates the data encoding of a digital sensor by converting x to an 8-bit integer
  clip: $x \leftarrow \texttt{max}(-128, \texttt{min}(x, 127))$.
  return $\texttt{int}(x)$
end procedure

4.4 Evaluation of the B^{EMD}

For each candidate model we use the hierarchical beta process $\mathfrak{Q}_a$ described below to generate on the order of $M_a \approx 100$ PPFs $\hat{q}_{a,1}, \ldots, \hat{q}_{a,M_a}$; the exact number of PPFs is determined automatically, by increasing the number M_a until the relative standard error on $\frac{1}{M_a}\sum_{i=1}^{M_a} R[\hat{q}_{a,i}]$ is below 2^{-5} (six such PPFs are shown as grey traces in Fig. 6). Each curve is integrated to obtain a value for the risk (equation (14)), such that the R_a distribution can be represented by the set $\{R[\hat{q}_{a,i}]\}_{i=1}^{M_a}$. We then use a kernel density estimate to visualise these distributions in Fig. 3; specifically we use the `univariate_kde` function provided by Holoviews [48] with default parameters. The function automatically determines the bandwidth.

4.5 Calibration for the neural response model

As described in our Results, the goal of *calibration* is twofold. First we want to align the value of B_{AB}^{EMD} with the probability that model A consistently has lower risk than model B under a variety of experimental conditions. Second, we want to ensure

that a decision to falsify based on B_{AB}^{EMD} is robust: it should hold for any reasonable distribution of experimental conditions (and therefore hopefully also for *unanticipated* experimental variations).

The calibration procedure involves fixing two candidate models and varying the model used to generate the data (i.e. varying $\mathcal{M}_{\mathrm{true}}$); we referred to this as an *epistemic distribution*. This process can be repeated for as many epistemic distributions and as many different pairs of candidate models as desired, until we are sufficiently confident in the robustness of our criterion.

For the neuron model, we consider four sources of experimental variability: variations in the distribution used to model observation noise ξ, variations in the strength (σ_o) of observation noise, as well as variations in the strength (σ_i) and correlation time (τ) of the external input I_{ext}. Each epistemic distribution Ω is therefore described by four distributions over hyperparameters:

Observation noise model One of *Gaussian* or *Cauchy*. The distributions are centered and σ_o is drawn from the distribution defined below. Note that this is the model used to *generate* a dataset $\mathcal{D}_{\mathrm{test}}$. The candidate models always evaluate their loss assuming a Gaussian observation model.

$$\textit{Gaussian:} \qquad p(\xi) = \frac{1}{\sqrt{2\pi\sigma}} \exp\left(-\frac{\xi^2}{2\sigma_o^2}\right)$$

$$\textit{Cauchy:} \qquad p(\xi) = \frac{2}{\pi\sigma\left[1 + \left(\frac{\xi^2}{\sigma_o/2}\right)\right]}$$

Observation noise strength σ_o

$$\textit{Low noise:} \qquad \log \sigma_o \sim \mathcal{N}(0.0\,\mathrm{mV}, (0.5\,\mathrm{mV})^2)$$

$$\textit{High noise:} \qquad \log \sigma_o \sim \mathcal{N}(1.0\,\mathrm{mV}, (0.5\,\mathrm{mV})^2)$$

External input strength σ_i The parameter σ_i sets the strength of the input noise such that $\langle I_{\mathrm{ext}}^2 \rangle = \sigma_i^2$.

$$\textit{Weak input:} \qquad \log \sigma_i \sim \mathcal{N}(-15.0\,\mathrm{mV}, (0.5\,\mathrm{mV})^2)$$

$$\textit{Strong input:} \qquad \log \sigma_i \sim \mathcal{N}(-10.0\,\mathrm{mV}, (0.5\,\mathrm{mV})^2)$$

External input correlation time τ The parameter τ sets the correlation time of the input noise such that $\langle I_{\mathrm{ext}}(t) I_{\mathrm{ext}}(t+s) \rangle = \sigma_i^2 e^{-s^2/2\tau^2}$.

$$\textit{Short correlation:} \qquad \log_{10} \tau \sim \mathrm{Unif}([0.1\,\mathrm{ms}, 0.2\,\mathrm{ms}])$$

$$\textit{Long correlation:} \qquad \log_{10} \tau \sim \mathrm{Unif}([1.0\,\mathrm{ms}, 2.0\,\mathrm{ms}])$$

We thus defined 2 statistical distributions for ξ, 2 distributions for σ_o, 2 distributions for τ, and 2 distributions for σ_i. Combined with three model pairs (see Fig. 7), this makes a total of $48 = 3\times2\times2\times2\times2$ possible epistemic distributions Ω, each of which can be identified by a tuple such as ($\mathcal{M}_A$ `vs` $\mathcal{M}_B$, `Cauchy`, `Low noise`, `Strong input`, `Long correlation`). Calibration results for each of these conditions are given in Fig. 1.

During calibration against an epistemic distribution Ω, drawing a dataset $\mathcal{D}_{\mathrm{test}}$ happens in two steps. First, we randomly draw a vector ω of epistemic parameters (i.e. hyperparameters) from Ω; for example $\omega = (\underbrace{-0.27\mathrm{mV}}_{\sigma_o}, \underbrace{47\mathrm{ms}}_{\tau}, \underbrace{0.003\mathrm{mV}}_{\sigma_i})$. Second, we use those parameters to generate the dataset $\mathcal{D}_{\mathrm{test}}$, composed in this case of data points $(t, \tilde{V}^{\mathrm{LP}}(t))$. We can then evaluate the loss Q (given by equation (6)) on those data points. Note that the loss does not depend on the epistemic parameters ω directly, but in general will involve parameters which are fitted to the simulated data. In short, the vector ω describes the parameters of a simulated experiment, while $\mathcal{D}_{\mathrm{test}}$ describes a particular outcome of that experiment. In theory we could generate multiple datasets with the same vector ω, but in practice it is more statistically efficient to draw a new experiment for each new dataset.

When choosing epistemic distributions, it is worth remembering that the goal of calibration is to empirically approximate a probability over experimental conditions. Thus choosing a distribution which can generate a large number of conditions – ideally an infinite number – will lead to better estimates. Here the use of continuous distributions for σ_o, σ_i and τ, and the fact that I_{ext} is a continuous process, helps us achieve this goal.

This calibration is an imperfect procedure, and how well it works depends on the quality of the candidate models and the choice of loss function. Here for example, the choice of a pointwise loss makes it sensitive to the timing of spikes; this tends to favour models which produce fewer spikes, since the penalty on a mis-timed spike is high. This is why in Fig. 7, in the $\mathcal{M}_A$ `vs` $\mathcal{M}_D$ comparison, we see a floor on the values of B_{AD}^{epis}. In short, some models have consistently lower loss even on random data, and so their risk – which is the expectation of their loss – is a priori lower. The bias we see in the $\mathcal{M}_A$ `vs` $\mathcal{M}_B$ comparison is likely due to a similar effect. (In this case because $\mathcal{M}_B$ is slightly better than $\mathcal{M}_A$ on average.)

4.6 The hierarchical beta process

In this work we identify the epistemic uncertainty of a model $\mathcal{M}_A$ with the variability of a stochastic process $\mathfrak{Q}_A$: realizations of $\mathfrak{Q}_A$ approximate the PPF of the model loss. In our Results we listed desiderata which $\mathfrak{Q}_A$ should satisfy and proposed that it be described as a hierarchical beta (HB) process. However we deferred providing a precise definition for $\mathfrak{Q}_A$; we do this now in the form of Algorithm 2. The rest of this section explains the theoretical justifications for each step of this generative algorithm for $\mathfrak{Q}_A$.

4.6.1 Relevant concepts of Wiener processes

Before introducing the HB process, let us first review a few key properties which stochastic processes must satisfy and which are covered in most standard introductions [49–51]. We use the well-known Wiener process to introduce properties and notation which will become useful when we define the HB process. Since our goal is to define a process for PPFs, we use Φ to denote the independent "domain" variable and restrict ourselves to 1-d processes for which $\Phi \in [0, 1]$.

For the Wiener process $\mathcal{W}$, each realization is a continuous function $W\colon [0,1] \to \mathbb{R}$. One way to approximate a realization of $\mathcal{W}$ is to first partition the interval into subintervals $[0, \Phi_1), [\Phi_1, \Phi_2), \ldots, [\Phi_n, 1)$ with $0 < \Phi_1 < \Phi_2 < \cdots < \Phi_n < 1$; for simplicity we will only consider equal-sized subintervals, so that $\Phi_k = k\,\Delta\Phi$ for some $\Delta\Phi \in \mathbb{R}$. We then generate a sequence of

Algorithm 2 Hierarchical beta process

Given

- q_A^*, c and δ_A^{EMD}, ▷ computed from data
- $N \in \mathbb{N}^+$, ▷ number of refinements
- $p(\hat{q}(0), \hat{q}(1))$, ▷ 2-d distribution over end points

generate a discretized realization $\hat{q}_A$.

Procedure:

▷ Initialize the procedure by drawing end point
1: **repeat**
2: **draw** $(\hat{q}(0), \hat{q}(1)) \sim p(\hat{q}(0), \hat{q}(1))$
3: **until** $\hat{q}(0) < \hat{q}(1)$ ▷ PPFs must be increasing
▷ Successively refine the interval
4: **for** $n \in 1, 2, \ldots, N$ **do** ▷ refinement levels
5: **for** $\Phi \in \{\mathcal{I}_\Phi\}^{(n)}$ **do** ▷ intermediate increments
6: **compute** r, v according to equations (56)
7: **solve** equations (58) to obtain α and β
8: **draw** $x_1 \sim \mathrm{Beta}(\alpha, \beta)$
9: $\hat{q}(\Phi + 2^{-n}) \leftarrow \hat{q}(\Phi) + \Delta\hat{q}_{\Delta\Phi}(\Phi) \cdot x_1$
10: **end for**
11: **end for**
12: **return** $(\hat{q}(\Phi) : \Phi \in \{\mathcal{I}_\Phi\}^{(N)})$

The quantities r and v computed on Line 6 conceptually represent the **r**atio between two sucessive increments and the **v**ariance of those increments.

independent random increments (one for each subinterval) $\{\Delta W_{\Delta\Phi}(0), \Delta W_{\Delta\Phi}(\Delta\Phi), \Delta W_{\Delta\Phi}(2\Delta\Phi), \ldots, \Delta W_{\Delta\Phi}(1-\Delta\Phi)\}$ and define the corresponding realization as

$$W(k\,\Delta\Phi) = W(0) + \sum_{l=0}^{k-1} \Delta W_{\Delta\Phi}(l\,\Delta\Phi) = W(0) + \Delta W_{\Delta\Phi}((k-1)\,\Delta\Phi)\,. \tag{41}$$

(Within each interval the function may be linearly interpolated, so that W is continuous.)

A *refinement* of a partition is obtained by taking each subinterval and further dividing it into smaller subintervals. For instance we can refine the unit interval $[0, 1)$ into a set of two subintervals, $[0, 2^{-1})$ and $[2^{-1}, 2^{-0})$. Let us denote these partitions $\{\mathcal{I}_\Phi\}^{(0)}$ and $\{\mathcal{I}_\Phi\}^{(1)}$ respectively. Repeating the process on each subinterval yields a sequence of ever finer refinements:

$$\begin{aligned}
\{\mathcal{I}_\Phi\}^{(0)} &:= \left\{ [\,0,\ 2^{-0}\,) \right\} \\
\{\mathcal{I}_\Phi\}^{(1)} &:= \left\{ [\,0,\ 2^{-1}\,),\ [\,2^{-1},\ 2^{-0}\,) \right\} \\
\{\mathcal{I}_\Phi\}^{(2)} &:= \left\{ [\,0,\ 2^{-2}\,),\ [\,2^{-2},\ 2^{-1}\,),\ [\,2^{-1},\ 3\cdot 2^{-2}\,),\ [\,3\cdot 2^{-2},\ 2^{-0}\,) \right\} \\
&\vdots \\
\{\mathcal{I}_\Phi\}^{(n)} &:= \left\{ [\,k\cdot 2^{-n},\ (k+1)\cdot 2^{-n}\,) \right\}_{k=0}^{2^n-1}\,.
\end{aligned} \tag{42}$$

With these definitions, for any $m \geq n$, $\{\mathcal{I}_\Phi\}^{(m)}$ is a refinement of $\{\mathcal{I}_\Phi\}^{(n)}$.

Later we will need to refer to the vector of new end points introduced at the n-th refinemement step. These are exactly the odd multiples of 2^{-n} between 0 and 1, which we denote $\{\Phi\}^{(n)}$:

$$\{\Phi\}^{(n)} := \left(2^{-n},\ 3\cdot 2^{-n},\ \ldots,\ (2^n-3)\cdot 2^{-n},\ (2^n-1)\cdot 2^{-n}\right). \tag{43}$$

Any random process must be *self-consistent* [28]: for small enough $\Delta\Phi$, the probability distribution at a point Φ must not depend on the level of refinement. For example, the Wiener process is defined such that the increments $\Delta W_{\Delta\Phi} \sim \mathcal{N}(0, \Delta\Phi)$ are independent; therefore

$$\begin{aligned}
&W(\Phi+2\Delta\Phi) \\
&= W(\Phi) + \Delta W_{2\Delta\Phi}(\Phi) = W(\Phi) + \Delta W_{\Delta\Phi}(\Phi) + \Delta W_{\Delta\Phi}(\Phi+\Delta\Phi) \\
&= W(\Phi) + \mathcal{N}(0, 2\Delta\Phi) = W(\Phi) + \mathcal{N}(0, \Delta\Phi) + \mathcal{N}(0, \Delta\Phi)\,.
\end{aligned} \tag{44}$$

It turns out that the combination of the Markovian and self-consistent properties set quite strong requirements on the stochastic increments, since they impose the square root scaling of the Wiener increment: $O(\Delta W_{\Delta\Phi}) = O(\sqrt{\Delta\Phi})$. (§II.C of Gillespie [28].)

While the Wiener process underlies much of stochastic theory, it is not suitable for defining a process $\mathfrak{Q}$ over PPFs. Indeed, it is not monotone by design, which violates one of our desiderata. Moreover, it has a built-in directionality in the form of accumulated increments. A clear symptom of this is that as Φ increases, the variance of $W(\Phi)$ also increases. (This follows immediately from equation (41) and the independence of increments.) Directionality makes sense if we think of W as modelling the diffusion of particles in space or time, but empirical PPFs are obtained by first sorting data samples according to their loss (see the definition of δ^{EMD}). Since samples of the loss arrive in no particular order, a process which samples PPFs should likewise have no intrinsic directionality in Φ.

4.6.2 *A hierarchical beta distribution is monotone, non-accumulating and self-consistent*

Constructing a stochastic process $\mathfrak{Q}$ which is *monotone* is relatively simple: one only needs to ensure that the random increments $\Delta\hat{q}_{\Delta\Phi}(\Phi)$ are non-negative.

Ensuring that those increments are *non-accumulating* requires more care, because that requirement invalidates most common definitions of stochastic processes. As described in our Results, we achieve this by defining $\mathfrak{Q}$ as a sequence of refinements, starting from a single increment for the entire interval, then doubling the number of increments (and halving their width) at each refinement step. In the rest of this subsection we give an explicit construction of this process and show that it is also *self-consistent*. (Altough in this work we consider only pairs of increments sampled from a beta distribution, in general one could consider other compositional distributions. Higher-dimensional distributions may allow to sample all increments simultaneously, if one can determine the conditions which ensure self-consistency.)

For an interval $\mathcal{I} = [\Phi, \Phi + \Delta\Phi)$, we suppose that the points $\hat{q}_A(\Phi)$ and $\hat{q}_A(\Phi + \Delta\Phi)$ are given. We define

$$\Delta\hat{q}(\mathcal{I}) \;=\; \Delta\hat{q}_{\Delta\Phi}(\Phi) \;:=\; \hat{q}_A(\Phi + \Delta\Phi) - \hat{q}_A(\Phi)\,, \tag{45}$$

then we draw a subincrement $\Delta\hat{q}_{\frac{\Delta\Phi}{2}}(\Phi)$, associated to the subinterval $[\Phi, \Phi + \Delta\Phi)$, from a scaled beta distribution:

$$\frac{1}{\Delta\hat{q}_{\Delta\Phi}(\Phi)} \Delta\hat{q}_{\frac{\Delta\Phi}{2}}(\Phi) := x_1 \sim \mathrm{Beta}(\alpha, \beta)\,. \tag{46}$$

(Refer to the subsection below for the definition of Beta(α,β).) The scaling is chosen so that

$$0 \le \underbrace{\Delta\hat{q}_{\frac{\Delta\Phi}{2}}(\Phi)}_{=x_1\Delta\hat{q}_{\Delta\Phi}(\Phi)} \le \Delta\hat{q}_{\Delta\Phi}(\Phi)\,. \tag{47}$$

The value of $\Delta\hat{q}_{\frac{\Delta\Phi}{2}}(\Phi)$ then determines the intermediate point:

$$\hat{q}_A(\Phi + \tfrac{\Delta\Phi}{2}) \leftarrow \hat{q}_A(\Phi) + \Delta\hat{q}_{\frac{\Delta\Phi}{2}}(\Phi)\,. \tag{48}$$

If desired, the complementary increment $\Delta\hat{q}_{\frac{\Delta\Phi}{2}}(\Phi + \frac{\Delta\Phi}{2})$ can be obtained as

$$\Delta\hat{q}_{\frac{\Delta\Phi}{2}}(\Phi + \tfrac{\Delta\Phi}{2}) = (1 - x_1)\Delta\hat{q}_{\Delta\Phi}(\Phi)\,. \tag{49}$$

Generalizing the notation to the entire $[0, 1)$ interval, we start from a sequence of increments associated to subintervals at refinement step n (recall equation (42)):

$$\begin{aligned}\{\Delta\hat{q}_{2^{-n}}\} &\coloneqq \{\Delta\hat{q}(\mathcal{I}) \quad : \quad \mathcal{I} \in \{\mathcal{I}_\Phi\}^{(n)}\} \\ &\overset{\text{def}}{=} \{\Delta\hat{q}_{2^{-n}}(\Phi) : [\Phi, \Phi + 2^{-n}) \in \{\mathcal{I}_\Phi\}^{(n)}\}\,.\end{aligned}$$

Applying the procedure just described, for each subinterval we draw x_1 and split the corresponding increment $\Delta\hat{q}_{2^{-n}}(\Phi) \in \{\Delta\hat{q}_{2^{-n}}\}$ into a pair $(\Delta\hat{q}_{2^{-n-1}}(\Phi), \Delta\hat{q}_{2^{-n-1}}(\Phi + 2^{-n-1}))$ of subincrements such that

$$\Delta\hat{q}_{2^{-n}}(\Phi) = \Delta\hat{q}_{2^{-n-1}}(\Phi) + \Delta\hat{q}_{2^{-n-1}}(\Phi + 2^{-n-1})\,. \tag{50}$$

The union of subincrements is then the next refinement step:

$$\{\Delta\hat{q}(\mathcal{I}) : \mathcal{I} \in \{\mathcal{I}_\Phi\}^{(n+1)}\} = \{\Delta\hat{q}_{2^{-n-1}}\}\,. \tag{51}$$

After n refinement steps, we thus obtain a function $\hat{q}(\Phi)$ defined at discrete points:

$$\hat{q}^{(n)}(k \cdot 2^{-n}) \coloneqq \hat{q}(0) + \sum_{l<k} \Delta\hat{q}_{2^{-n}}(l \cdot 2^{-n})\,, \tag{52}$$

which we extend to the entire interval $[0, 1)$ by linear interpolation; see Fig. 6**d** for an illustration. In practice we found that computations (specifically the risk computed by integrating $\hat{q}^{(n)}(\Phi)$) converge after about eight refinement steps.

This procedure has the important property that once a point is sampled, it does not change on further refinements:

$$\hat{q}^{(n)}(k \cdot 2^{-n}) = \hat{q}^{(m)}(k \cdot 2^{-n})\,, \quad \forall m \ge n\,, \tag{53}$$

which follows from equation (50). Recall now that, as stated above, a process is self-consistent if "for small enough $\Delta\Phi$, the probability distribution at a point Φ [does] not depend on the level of refinement". Since equation (53) clearly satisfies that requirement, we see that the process obtained after infinitely many refinement steps is indeed self-consistent. We thus define the *hierarchical beta (HB) process* $\mathfrak{Q}_A$ as

$$p(\hat{q} \mid \mathfrak{Q}_A) \coloneqq p\Big(\hat{q} = \lim_{n\to\infty} \hat{q}^{(n)} \;\Big|\; q^*_A, \delta^{\text{EMD}}_A, c\Big)\,. \tag{54}$$

To complete the definition of $\mathfrak{Q}_A$, we need to specify how we choose the initial end points $\hat{q}_A(0)$ and $\hat{q}_A(1)$. In our code implementation, they are drawn from normal distributions $\mathcal{N}(q^*(\Phi), \sqrt{c}\,\delta^{\text{EMD}}_A(\Phi)^2)$ with $\Phi \in \{0, 1\}$, where again c is determined via our proposed calibration procedure; this is simple and convenient, but otherwise arbitrary. We also need to explain how we choose the beta parameters α and β, which is the topic of the next subsection.

4.6.3 *Choosing beta distribution parameters*

All HB processes are monotone, continuous and self-consistent, but within this class there is still a lot of flexibility: since α and β are chosen independently for each subinterval and increment, we can mold $\mathfrak{Q}_A$ into a wide variety of statistical shapes. We use this flexibility to satisfy the two remaining desiderata: a) that $\hat{q}_A(\Phi)$ realizations track $q^*_A(\Phi)$ over $\Phi \in [0, 1]$; and b) that the variability of $\hat{q}_A(\Phi)$ be proportional to $\delta^{\text{EMD}}_A(\Phi)$. It is the goal of this subsection to give a precise mathematical meaning to those requirements.

Let $x_1 \sim \text{Beta}(\alpha, \beta)$ and $x_2 = 1 - x_1$. (The density function of a beta distribution is given in equation (18).) The mean and variance of x_1 are

$$\mathbb{E}[x_1] = \frac{\alpha}{\alpha + \beta}\,, \tag{55a}$$

$$\mathbb{V}[x_1] = \frac{\alpha\beta}{(\alpha + \beta)^2(\alpha + \beta + 1)}\,. \tag{55b}$$

For a given Φ, it may seem natural to select α and β by matching $\mathbb{E}[x_1]$ to $q^*_A(\Phi)$ and $\mathbb{V}[x_1]$ to $c{\cdot}(\delta^{\text{EMD}}_A(\Phi))^2$. However both equations are tightly coupled, and we found that numerical solutions were unstable and unsatisfactory; in particular, it is not possible to make the variance large when $\mathbb{E}[x_1]$ approaches either 0 or 1 (otherwise the distribution of x_1 would exceed $[0, 1]$).

Much more practical is to consider moments with respect to the Aitchison measure; as mentioned previously, the Aitchison measure first maps the bounded interval $[0, 1]$ to the unbounded space $\mathbb{R}$ with a logistic transformation, then computes moments in the unbounded space. The first two such moments are called the *centre* and the *metric variance* [29, 30]; for the beta distribution, they are given by (reproduced from 19)

$$\mathbb{E}_a[(x_1, x_2)] = \frac{1}{e^{\psi(\alpha)} + e^{\psi(\beta)}}(e^{\psi(\alpha)}, e^{\psi(\beta)})\,, \tag{19a}$$

$$\text{Mvar}[(x_1, x_2)] = \frac{1}{2}(\psi_1(\alpha) + \psi_1(\beta))\,, \tag{19b}$$

where ψ and ψ_1 are the digamma and trigamma functions respectively. The centre and metric variance are known to be more natural statistics for compositional distributions, and this is what we found in practice. Therefore we will relate q^*_A to the centre, and $\sqrt{c}\,\delta^{\text{EMD}}_A$ to the square root of the metric variance.

To be precise, suppose that we have already selected a set of increments $\{\Delta\hat{q}_{2^{-n}}\}$ over the domain $\{k \cdot 2^{-n}\}_{k=0}^{n-1}$, and wish to produce the refinement $\{\Delta\hat{q}_{2^{-n-1}}\}$. For each Φ in $\{k \cdot 2^{-n}\}_{k=0}^{n-1}$ we define

$$r \coloneqq \frac{q^*_A(\Phi + 2^{-n-1}) - q^*_A(\Phi)}{q^*_A(\Phi + 2^{-n}) - q^*_A(\Phi + 2^{-n-1})}\,, \tag{56a}$$

$$v \coloneqq 2\,c\left(\delta^{\text{EMD}}_A(\Phi + 2^{-n-1})\right)^2. \tag{56b}$$

The value r is the ratio of subincrements of $\Delta q^*_{2^{-n}}(\Phi)$. Since we want $\hat{q}_A$ to track q^*_A, it makes sense to expect r to also approximate the ratio of subincrements of $\Delta\hat{q}_{2^{-n}}(\Phi)$. Identifying

$$r \leftrightarrow \frac{\mathbb{E}_a[x_1]}{\mathbb{E}_a[x_2]} \quad \text{and} \quad v \leftrightarrow 2 \cdot \text{Mvar}[(x_1, x_2)]\,, \tag{57}$$

and substituting into equations (19) then leads to the following system of equations:

$$\psi(\alpha) - \psi(\beta) = \ln r \tag{58a}$$

$$\ln[\psi_1(\alpha) + \psi_1(\beta)] = \ln v\,, \tag{58b}$$

which we can solve to yield the desired parameters α and β for each subinterval in $\{\mathcal{I}_\Phi\}^{(n)}$.

In summary, although the justification is somewhat technical, the actual procedure for obtaining α and β is quite simple: first compute r and v following equations (56), then solve equations (58).

4.7 Expressions for other model criteria

We list below the expressions for the other model criteria against which we compare the EMD criterion in Table 2. More details can also be found in the computational notebooks published alongside this paper [52].

Conventions we use in this section:

- $\mathcal{D}$: Training dataset used to fit the model.
- L: Number of data samples in $\mathcal{D}$.
- $(\lambda_i, \mathcal{B}_i)$: Sample in $\mathcal{D}$.
- $(\lambda'_j, \mathcal{B}'_j)$: Additional sample not in $\mathcal{D}$ (i.e. a test sample).
- $\hat{\sigma}, \hat{T}$: Estimates of σ and T obtained by maximizing the likelihood on $\mathcal{D}$.

EMD criterion

$$\log_{10} \underline{B}^{\mathrm{EMD}}_{AB;c} \coloneqq \log_{10} B^{\mathrm{EMD}}_{AB;c} - \log_{10}(1 - B^{\mathrm{EMD}}_{AB;c}) ,$$

where $A = \mathcal{M}_\mathrm{P}$ and $B = \mathcal{M}_\mathrm{RJ}$. (Repeated from equation (35).)

Loss function As we did for the neuron model, we define the loss of a point $(\lambda_i, \mathcal{B}_i)$ as the negative log likelihood given that data point. Since the candidate models assume Gaussian noise (equation (33)), this is simply

$$\begin{aligned} Q_a(\mathcal{B}_i \mid \lambda_i, \sigma, T) &= -\log p\Big(\mathcal{B} \;\Big|\; \mathcal{B}_a(\lambda; T), \sigma\Big) \\ &= \log \sqrt{2\pi}\sigma + \frac{(\mathcal{B} - \mathcal{B}_a(\lambda; T))^2}{2\sigma^2} . \end{aligned} \tag{59}$$

Here the subscript a is used to indicate whether we use predictions from the Rayleigh-Jeans (equation (30)) or Planck (equation (31)) model.

Log likelihood function Since we defined the loss as the negative log likelihood, one way to express the log likelihood for the whole dataset is simply as the negative total loss:

$$\ell_a(\sigma, T) \coloneqq \sum_{i=1}^{L} -Q_a(\mathcal{B}_i \mid \lambda_i, \sigma, T) . \tag{60}$$

Risk The risk is the expectation of the loss under the true model, so we have

$$R_a \coloneqq \Big\langle Q_a\Big(\mathcal{B}'_j \mid \lambda'_j, \hat{\sigma}_a, \hat{T}_a\Big)\Big\rangle_{\lambda'_j, \mathcal{B}'_j \sim \mathcal{M}_\mathrm{true}} , \tag{61}$$

$$\log_{10} \underline{B}^R \coloneqq -R_\mathrm{P} + R_\mathrm{RJ} \;/\; \log 10 , \qquad \text{(repeated from (36))}$$

where $\lambda'_j, \mathcal{B}'_j \sim \mathcal{M}_\mathrm{true}$ indicates that λ'_j and $\mathcal{B}'_j$ are random variables with the same probability as the data. The division by $\log 10$ converts the basis of the logarithms from e to 10.

Since in this case we know $\mathcal{M}_\mathrm{true}$, the expectation can be computed exactly. We did this by generating a very large number of data samples ($L = 2^{12}$) and computing the empirical average of the loss:

$$R_a \approx -\frac{1}{L} \ell_a(\hat{\sigma}_a, \hat{T}_a) . \tag{62}$$

Bayesian prior The Bayesian calculations require a prior on the parameters σ and T. We used a simple prior which factorizes into two independent distributions:

$$\begin{aligned} \pi\Big(\log_2 \sigma\Big) &\sim \mathrm{Unif}\Big(\Big[\log_2 2^9, \log_2 2^{14}\Big]\Big) , \\ \pi\Big(\log_2 T\Big) &\sim \mathrm{Unif}\Big(\Big[\log_2 1000, \log_2 5000\Big]\Big) . \end{aligned} \tag{63}$$

Here T is expressed in Kelvin and σ has units $\mathrm{kW} \cdot \mathrm{m}^{-2} \cdot \mathrm{nm}^{-1} \cdot \mathrm{sr}^{-1}$. We chose log uniform distributions because these are more appropriate for parameters which are strictly positive and which can span multiple scales: the logarithmic scaling captures the fact that the difference between 1000 K and 1001 K is more significant than the difference between 5000 K and 5001 K. Likewise for differences in the parameter σ at opposite ends of its range.

We also repeated calculations with much tighter prior ranges (2^9–2^{10} for σ, and 3900–4100 for T) and found very similar values (within 1% of those reported in Table 2).

Expected log pointwise posterior predictive density (elpd)

$$\mathrm{elpd}_a \coloneqq \Big\langle \log_{10} p(\lambda'_j, \mathcal{B}'_j \mid a, \mathcal{D})\Big\rangle_{\lambda'_j, \mathcal{B}'_j \sim \mathcal{M}_\mathrm{true}} \tag{64}$$

$$\log_{10} B^{\mathrm{elpd}} \coloneqq \mathrm{elpd}_\mathrm{P} - \mathrm{elpd}_\mathrm{RL} . \tag{65}$$

Note p in equation (64) is a posterior density, and therefore evaluating it involves integrating over the prior:

$$p(\lambda'_j, \mathcal{B}'_j \mid a, \mathcal{D}) = \iint d\sigma dT \, \pi_\sigma(\sigma) \pi_T(T) \; p(\lambda'_j, \mathcal{B}'_j \mid a, \mathcal{D}, \sigma, T) . \tag{66}$$

Relative likelihood and AIC The relative likelihood is given by

$$\log_{10} B^l \coloneqq \ell_\mathrm{P}(\hat{\sigma}_\mathrm{P}, \hat{T}_\mathrm{P}) - \ell_\mathrm{RL}(\hat{\sigma}_\mathrm{P}, \hat{T}_\mathrm{P}) \;/\; \log 10 , \tag{67}$$

while the difference between the AIC criteria of both models is (we use here the fact that both models have the same number of parameters)

$$\Delta AIC \coloneqq 2\ell_\mathrm{P}(\hat{\sigma}_\mathrm{P}, \hat{T}_\mathrm{P}) - 2\ell_\mathrm{RL}(\hat{\sigma}_\mathrm{P}, \hat{T}_\mathrm{P}) . \tag{68}$$

Since the two are equivalent up to a factor $2 \log 10$, the trends we see with the likelihood ratio therefore also occur with the AIC.

(The factor 2 in the AIC is meant to allow it to be interpreted – under certain assumptions – as a draw from a χ^2 distribution. This correspondence however is not required when interpreting Table 2.)

Model evidence The model evidence is used to compute the Bayes factors. It is the expectation of the likelihood of the data – $\mathcal{D} = \{\lambda_i, \mathcal{B}_i\}_{i=1}^L$ – under the prior for T and σ:

$$\begin{aligned} \mathcal{E}_a &\coloneqq \iint d\sigma dT \, \pi_\sigma(\sigma) \pi_T(T) \; p\Big(\{\lambda_i, \mathcal{B}_i\}_{i=1}^L \mid a, \sigma, T\Big) \\ &= \iint d\sigma dT \, \pi_\sigma(\sigma) \pi_T(T) \ell_a(\sigma, T) \; . \end{aligned} \tag{69}$$

The likelihood $p\Big(\{\lambda_i, \mathcal{B}_i\}_{i=1}^{L} \mid a, \sigma, T\Big)$ is given by the Gaussian observation model.

Bayes factor

$$\log_{10} B^B := \log_{10} \mathcal{E}_{\mathrm{P}} - \log_{10} \mathcal{E}_{\mathrm{RL}} \,. \tag{70}$$

Code availability

All source code used to produce the figures in this paper is available as a collection of Jupyter notebooks [52]. Additional Python code for simulating the neuron circuit model [45] and generating colored noise [46] is also available.

One advantage of our approach is that many of the computation steps can be automated. Given a set of observed data $\mathcal{D}_{\text{test}}$, a generative model $\mathcal{M}_A$, a loss fonction Q and sensitivity parameter $c \in \mathbb{R}$, a program can automatically compute $\tilde{q}_A$, q_A^* and δ_A^{EMD}, then draw samples from the R_A-distribution. In other words, all the steps represented by downward facing arrows on the right of Fig. 1 require only a one-time software implementation, which we provide as the Python package `emd-falsify` [18], available on the Python Packaging Index (PyPI).

The `emd-falsify` package also provides utilities to help execute calibration experiments.

References

1. Chmiela, S. *et al.* Machine Learning of Accurate Energy-Conserving Molecular Force Fields. *Science Advances* **3,** e1603015. doi:10.1126/sciadv.1603015 (May 2017).
2. René, A., Longtin, A. & Macke, J. H. Inference of a Mesoscopic Population Model from Population Spike Trains. *Neural Computation* **32,** 1448–1498. ISSN: 0899-7667. doi:10.1162/neco_a_01292 (June 2020).
3. Gu, M., Fang, X. & Luo, Y. Data-Driven Model Construction for Anisotropic Dynamics of Active Matter. *PRX Life* **1,** 013009. doi:10.1103/PRXLife.1.013009 (Aug. 2023).
4. Beven, K. & Freer, J. Equifinality, Data Assimilation, and Uncertainty Estimation in Mechanistic Modelling of Complex Environmental Systems Using the GLUE Methodology. *Journal of Hydrology* **249,** 11–29. ISSN: 0022-1694. doi:10.1016/S0022-1694(01)00421-8 (Aug. 2001).
5. Tarantola, A. Popper, Bayes and the Inverse Problem. *Nature Phys* **2,** 492–494. ISSN: 1745-2481. doi:10.1038/nphys375 (Aug. 2006).
6. Prinz, A. A., Bucher, D. & Marder, E. Similar Network Activity from Disparate Circuit Parameters. *Nature Neuroscience* **7,** 1345–1352. ISSN: 1097-6256, 1546-1726. doi:10.1038/nn1352 (Dec. 2004).
7. Beven, K. & Binley, A. The Future of Distributed Models: Model Calibration and Uncertainty Prediction. *Hydrological Processes* **6,** 279–298. ISSN: 1099-1085. doi:10.1002/hyp.3360060305 (1992).
8. Stedinger, J. R., Vogel, R. M., Lee, S. U. & Batchelder, R. Appraisal of the Generalized Likelihood Uncertainty Estimation (GLUE) Method. *Water Resources Research* **44.** ISSN: 1944-7973. doi:10.1029/2008WR006822 (2008).
9. Beven, K. & Smith, P. Concepts of Information Content and Likelihood in Parameter Calibration for Hydrological Simulation Models. *Journal of Hydrologic Engineering* **20,** A4014010. ISSN: 1943-5584. doi:10.1061/(ASCE)HE.1943-5584.0000991 (Jan. 2015).
10. Kennedy, M. C. & O'Hagan, A. Bayesian Calibration of Computer Models. *Journal of the Royal Statistical Society: Series B (Statistical Methodology)* **63,** 425–464. ISSN: 1467-9868. doi:10.1111/1467-9868.00294 (2001).
11. Kiureghian, A. D. & Ditlevsen, O. Aleatory or Epistemic? Does It Matter? *Structural Safety. Risk Acceptance and Risk Communication* **31,** 105–112. ISSN: 0167-4730. doi:10.1016/j.strusafe.2008.06.020 (Mar. 2009).
12. Gal, Y., Hron, J. & Kendall, A. *Concrete Dropout* in *Advances in Neural Information Processing Systems* **30** (2017).
13. Hüllermeier, E. & Waegeman, W. Aleatoric and Epistemic Uncertainty in Machine Learning: An Introduction to Concepts and Methods. *Mach Learn* **110,** 457–506. ISSN: 1573-0565. doi:10.1007/s10994-021-05946-3 (Mar. 2021).
14. List, F., Rodd, N. L., Lewis, G. F. & Bhat, I. Galactic Center Excess in a New Light: Disentangling the γ-Ray Sky with Bayesian Graph Convolutional Neural Networks. *Phys. Rev. Lett.* **125,** 241102. doi:10.1103/PhysRevLett.125.241102 (Dec. 2020).
15. Kahle, L. & Zipoli, F. Quality of Uncertainty Estimates from Neural Network Potential Ensembles. *Phys. Rev. E* **105,** 015311. doi:10.1103/PhysRevE.105.015311 (Jan. 2022).
16. Gelman, A. & Yao, Y. Holes in Bayesian Statistics. *J. Phys. G: Nucl. Part. Phys.* **48,** 014002. ISSN: 0954-3899, 1361-6471. doi:10.1088/1361-6471/abc3a5 (Jan. 2021).
17. Gonçalves, P. J. *et al.* Training Deep Neural Density Estimators to Identify Mechanistic Models of Neural Dynamics. *eLife* **9** (eds Huguenard, J. R., O'Leary, T. & Goldman, M. S.) e56261. ISSN: 2050-084X. doi:10.7554/eLife.56261 (Sept. 2020).
18. René, A. *EMD-falsify v1.0.0* Aug. 2024. doi:10.5281/zenodo.13287994.
19. Vehtari, A., Gelman, A. & Gabry, J. Practical Bayesian Model Evaluation Using Leave-One-out Cross-Validation and WAIC. *Stat Comput* **27,** 1413–1432. ISSN: 1573-1375. doi:10.1007/s11222-016-9696-4 (Sept. 2017).
20. Gelman, A. *et al. Bayesian Data Analysis* ISBN: 978-1-4398-9822-2 (CRC Press, Boca Raton, 2014).
21. Vapnik, V. *Principles of Risk Minimization for Learning Theory* in *Advances in Neural Information Processing Systems* **4** (1992).
22. Vapnik, V. N. *The Nature of Statistical Learning Theory* ISBN: 978-1-4757-3264-1 (Springer New York : Imprint : Springer, New York, NY, 2000).

23. De Silva, B. M., Higdon, D. M., Brunton, S. L. & Kutz, J. N. Discovery of Physics From Data: Universal Laws and Discrepancies. *Frontiers in Artificial Intelligence* **3.** ISSN: 2624-8212. doi:10.3389/frai.2020.00025 (2020).
24. Yu, B. Stability. *Bernoulli* **19.** ISSN: 1350-7265. doi:10.3150/13-BEJSP14 (Sept. 2013).
25. De Schuymer, B., De Meyer, H. & De Baets, B. Cycle-Transitive Comparison of Independent Random Variables. *Journal of Multivariate Analysis* **96,** 352–373. ISSN: 0047-259X. doi:10.1016/j.jmva.2004.10.011 (Oct. 2005).
26. Baets, B. D. & Meyer, H. D. in *Perception-Based Data Mining and Decision Making in Economics and Finance* (eds Batyrshin, I., Kacprzyk, J., Sheremetov, L. & Zadeh, L. A.) 261–274 (Springer, Berlin, Heidelberg, 2007). ISBN: 978-3-540-36247-0. doi:10.1007/978-3-540-36247-0_10.
27. Davison, A. C. & Hinkley, D. V. *Bootstrap Methods and Their Application* ISBN: 978-0-521-57471-6. doi:10.1017/CBO9780511802843 (Cambridge University Press, Cambridge, 1997).
28. Gillespie, D. T. The Mathematics of Brownian Motion and Johnson Noise. *American Journal of Physics* **64,** 225–240. ISSN: 0002-9505, 1943-2909. doi:10.1119/1.18210 (Mar. 1996).
29. Mateu-Figueras, G., Monti, G. S. & Egozcue, J. J. in *Advances in Compositional Data Analysis: Festschrift in Honour of Vera Pawlowsky-Glahn* (eds Filzmoser, P., Hron, K., Martín-Fernández, J. A. & Palarea-Albaladejo, J.) 61–82 (Springer International Publishing, Cham, 2021). ISBN: 978-3-030-71175-7. doi:10.1007/978-3-030-71175-7_4.
30. Pawlowsky-Glahn, V. & Egozcue, J. J. Geometric Approach to Statistical Analysis on the Simplex. *Stochastic Environmental Research and Risk Assessment* **15,** 384–398. ISSN: 1436-3259. doi:10.1007/s004770100077 (Oct. 2001).
31. Mateu-Figueras, G. & Pawlowsky-Glahn, V. *The Dirichlet Distribution with Respect to the Aitchison Measure on the Simplex - a First Approach* in *Proceeding of the 2nd International Workshop on Compositional Data Analysis* (Girona, Oct. 2005).
32. Trotta, R. Bayes in the Sky: Bayesian Inference and Model Selection in Cosmology. *Contemporary Physics* **49,** 71–104. ISSN: 0010-7514. doi:10.1080/00107510802066753 (Mar. 2008).
33. Marco Taboga. in *Lectures on Probability Theory and Mathematical Statistics* Online appendix (Kindle Direct Publishing, 2021).
34. Beven, K. & Binley, A. GLUE: 20 Years On. *Hydrol. Process.* **28,** 5897–5918. ISSN: 0885-6087, 1099-1085. doi:10.1002/hyp.10082 (Nov. 2014).
35. Prinz, A. A., Billimoria, C. P. & Marder, E. Alternative to Hand-Tuning Conductance-Based Models: Construction and Analysis of Databases of Model Neurons. *Journal of Neurophysiology* **90,** 3998–4015. ISSN: 0022-3077. doi:10.1152/jn.00641.2003 (Dec. 2003).
36. Nowotny, T., Szücs, A., Levi, R. & Selverston, A. I. Models Wagging the Dog: Are Circuits Constructed with Disparate Parameters? *Neural Computation* **19,** 1985–2003. ISSN: 0899-7667. doi:10.1162/neco.2007.19.8.1985 (Aug. 2007).
37. Xu, K. & Darve, E. Physics Constrained Learning for Data-Driven Inverse Modeling from Sparse Observations. *Journal of Computational Physics* **453,** 110938. ISSN: 0021-9991. doi:10.1016/j.jcp.2021.110938 (Mar. 2022).
38. Toni, T., Welch, D., Strelkowa, N., Ipsen, A. & Stumpf, M. P. Approximate Bayesian Computation Scheme for Parameter Inference and Model Selection in Dynamical Systems. *Journal of The Royal Society Interface* **6,** 187–202. doi:10.1098/rsif.2008.0172 (July 2008).
39. Chen, S., Mira, A. & Onnela, J.-P. Flexible Model Selection for Mechanistic Network Models. *Journal of Complex Networks* **8,** cnz024. ISSN: 2051-1329. doi:10.1093/comnet/cnz024 (Apr. 2020).
40. Arendt, P. D., Apley, D. W. & Chen, W. Quantification of Model Uncertainty: Calibration, Model Discrepancy, and Identifiability. *Journal of Mechanical Design* **134.** ISSN: 1050-0472. doi:10.1115/1.4007390 (Sept. 2012).
41. Kuhn, T. S. *The Structure of Scientific Revolutions* Fourth edition. ISBN: 978-0-226-45811-3 (The University of Chicago Press, Chicago ; London, 2012).
42. Swigon, D., Stanhope, S. R., Zenker, S. & Rubin, J. E. On the Importance of the Jacobian Determinant in Parameter Inference for Random Parameter and Random Measurement Error Models. *SIAM/ASA J. Uncertainty Quantification* **7,** 975–1006. doi:10.1137/17M1114405 (Jan. 2019).
43. Talts, S., Betancourt, M., Simpson, D., Vehtari, A. & Gelman, A. Validating Bayesian Inference Algorithms with Simulation-Based Calibration. *arXiv:1804.06788 [stat]* (Apr. 2018).
44. Modrák, M. *et al.* Simulation-Based Calibration Checking for Bayesian Computation: The Choice of Test Quantities Shapes Sensitivity. *Bayesian Analysis* **Advance publication,** 28. ISSN: 1936-0975, 1931-6690. doi:10.1214/23-BA1404 (2023).
45. René, A. *Efficient and Flexible Simulator of the Lobster Pyloric Circuit* July 2024. doi:10.5281/zenodo.12797200.
46. René, A. *Solid Colored Noise Using Sparse Convolutions* July 2024. doi:10.5281/zenodo.12805191.
47. Lewis, J. P. *Algorithms for Solid Noise Synthesis* in *Proceedings of the 16th Annual Conference on Computer Graphics and Interactive Techniques* (New York, NY, USA, July 1989), 263–270. ISBN: 978-0-89791-312-6. doi:10.1145/74333.74360.
48. Rudiger, P. *et al. Holoviz/Holoviews: Version 1.18.1* Nov. 2023. doi:10.5281/zenodo.10089811.
49. Gardiner, C. W. *Handbook of Stochastic Methods: For Physics, Chemistry and the Natural Sciences ; with 29 Figures Springer Series in Synergetics* **13.** ISBN: 978-3-540-11357-7 (Springer, Berlin, 1983).

50. Risken, H. *The Fokker-Planck Equation: Methods of Solution and Applications* 2nd ed. *Springer Series in Synergetics* **v. 18.** ISBN: 978-0-387-50498-8 (Springer-Verlag, Berlin ; New York, 1989).
51. Horsthemke, W. & Lefever, R. *Noise-Induced Transitions: Theory and Applications in Physics, Chemistry, and Biology* 2. print. *Springer Series in Synergetics* **15.** ISBN: 978-3-540-11359-1 (Springer, Berlin, 2006).
52. René (code available on request; will be published upon acceptance). *Code for the EMD Falsification Paper* Jan. 2024. doi:10.5281/zenodo.0000000.
53. Conrey, B., Gabbard, J., Grant, K., Liu, A. & Morrison, K. E. Intransitive Dice. *Mathematics Magazine* **89,** 133–143. ISSN: 0025-570X, 1930-0980. doi:10.4169/math.mag.89.2.133 (Apr. 2016).

Acknowledgements

We thank Anno Kürth, Aitor Morales-Gregorio, Günther Palm, Moritz Helias, Jan Bölts, Abel Jansma, Thomas Nowotny and Manfred Opper for helpful comments and discussions.

This work was partly supported by the German Federal Ministry for Education and Research (BMBF Grant 01IS19077A), the Canadian National Research Council (NSERC) and the government of Ontario (OGS).

Author contributions

A.R developed the theory, wrote the software implementations and the first draft of the manuscript. A.R and A.L. discussed the results and revised the manuscript.

Additional information

Competing interests: The authors declare no competing interests.

Epistemically robust selection of fitted models – Supplementary Information –

Supplementary Figures

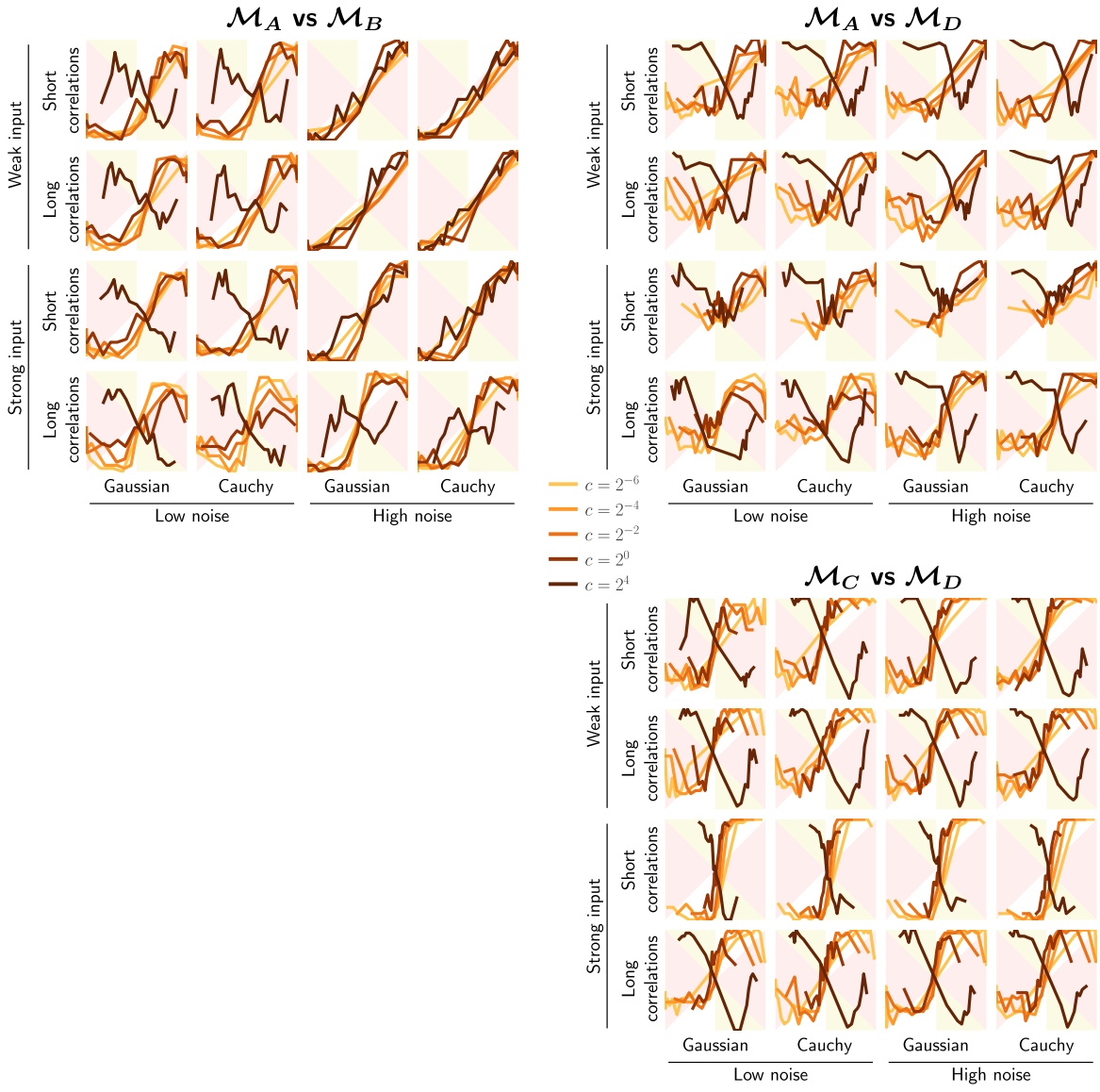

Supplementary Figure 1: **Additional calibration curves for the neuron model**, computed following the procedure described in section Calibrating and validating the B^{EMD} of the main text. As in Fig. 7, each curve summarizes 512 simulated experiments with datasets of size 4000. The regions depicted in red and yellow are those where equation (28) is violated.

Supplementary Methods

Transitivity of B^{EMD} comparisons

Given three independent random variables R_A, R_B and R_C, define the probabilities

$$\underbrace{P(R_A < R_B)}_{=:B_{AB}} \qquad \underbrace{P(R_B < R_C)}_{=:B_{BC}} \qquad \underbrace{P(R_C < R_A)}_{=:B_{CA}} .$$

For some threshold ϵ, we would like these to satisfy a transitivity relation of the form

$$\left.\begin{aligned} B_{AB} > \epsilon \\ B_{BC} > \epsilon \end{aligned}\right\} \Rightarrow B_{AC} < \epsilon , \tag{S1}$$

as this would reduce the required number of pairwise comparisons between models (see section Model discrepancy as a baseline for epistemic uncertainty, Table 1 and equation (11) in the main text).

It is known that equation (S1) does not hold for $\epsilon = \frac{1}{2}$; classic counterexamples in this case are non-transitive dice [53]. However, the set of probabilities $\mathcal{S} := \{B_{AB}, B_{BC}, B_{CA}\}$ *does* satisfy a property known as *dice-transitivity* [25], from which one can derive that equation (S1) holds when $\epsilon = \varphi^{-1}$, where φ is the golden ratio. This result appears as a comment within a more general proof in Baets & Meyer [26], but to our knowledge has otherwise remained unknown. We provide a short self-contained derivation below, for the convenience of the reader.

The definition of dice-transitivity is obtained by substituting equation (9) of De Schuymer *et al.* [25] into equation (6) of the same reference. For our purposes we are interested in the resulting upper bound

$$\alpha - 1 \leq -\beta\gamma , \tag{S2}$$

where α, β, and γ are respectively the lowest, middle and highest value of $\mathcal{S}$. In other words, $\{\alpha, \beta, \gamma\} = \mathcal{S}$ and

$$\alpha \leq \beta \leq \gamma . \tag{S3}$$

Suppose that, as given in equation (11), we have

$$B_{AB} > \varphi^{-1} \quad \text{and} \quad B_{BC} > \varphi^{-1} . \tag{S4}$$

We wish to use equation (S2) to establish an upper bound on B_{CA}. We do not know a priori how the probabilities are ordered, so we consider the six possible cases:

B_{AB}	B_{BC}	B_{CA}
α	β	γ
β	α	γ
α	γ	β
γ	α	β
β	γ	α
γ	β	α

(S5)

Cases $\alpha\beta\gamma$ and $\beta\alpha\gamma$ The assumptions of equation (S4) translate to $\alpha > \varphi^{-1}$ and $\beta > \varphi^{-1}$. We seek a bound on γ. Rearranging equation (S2), we then have

$$\gamma \leq \frac{1-\alpha}{\beta} < \frac{1-\varphi^{-1}}{\varphi^{-1}} = \frac{-1+\sqrt{5}}{2} = \varphi^{-1} , \tag{S6}$$

which contradicts equation (S3).

Cases $\alpha\gamma\beta$ and $\gamma\alpha\beta$ The argument is exactly analogous, except that we seek a bound on β. We get

$$\beta \leq \frac{1-\alpha}{\gamma} < \frac{1-\varphi^{-1}}{\varphi^{-1}} = \varphi^{-1} , \tag{S7}$$

which again contradicts equation (S3).

Therefore the only possible cases are $\beta\gamma\alpha$ and $\gamma\beta\alpha$, which means that B_{CA} must be the smallest of the three probabilities. These two final cases provide the upper bound on B_{CA}:

Cases $\beta\gamma\alpha$ and $\gamma\beta\alpha$ We seek a bound on α. Rearranging equation (S2) one more time yields

$$\alpha \leq 1 - \beta\gamma < 1 - \varphi^{-2} = \varphi^{-1} . \tag{S8}$$

Thus equation (S1) holds for $\epsilon = \varphi^{-1}$, which we gave in the main text as equation (11).

More generally, we conclude from equation (S8) that for any falsification threshold $\epsilon > \varphi^{-1}$,

$$\left.\begin{aligned} B^{\mathrm{EMD}}_{AB;c} > \epsilon \\ B^{\mathrm{EMD}}_{BC;c} > \epsilon \end{aligned}\right\} \Rightarrow B^{\mathrm{EMD}}_{AC;c} < 1 - \epsilon^2 . \tag{S9}$$